Nuclear Inst. and Methods in Physics Research, A 964 (2020) 163791

Contents lists available at ScienceDirect

Nuclear Inst. and Methods in Physics Research, A

journal homepage: www.elsevier.com/locate/nima

The CLAS12 Ring Imaging Cherenkov detector

M. Contalbrigo [a,*], V. Kubarovsky [f], M. Mirazita [b], P. Rossi [f,b], G. Angelini [b,j], H. Avakian [f], K. Bailey [g], I. Balossino [a], L. Barion [a], F. Benmokhtar [h], P. Bonneau [f], W. Briscoe [j], W. Brooks [k], E. Cisbani [c], C. Cuevas [f], P. Degtiarenko [f], C. Dickover [f], K. Hafidi [g], K. Joo [i], A. Kim [i], T. Lemon [f], V. Lucherini [b], R. Malaguti [a], R. Montgomery [b], A. Movsisyan [a], P. Musico [d], T. O'Connor [g], D. Orecchini [b], L.L. Pappalardo [a], C. Pecar [h], R. Perrino [e], B. Raydo [f], S. Tomassini [b], M. Turisini [a,b], A. Yegneswaran [f]

[a] INFN Sezione di Ferrara and University of Ferrara, 44100 Ferrara, Italy
[b] INFN Laboratori Nazionali di Frascati, 00044 Frascati, Italy
[c] INFN Sezione di Roma1 - Gruppo Collegato Sanità and Italian National Institute of Health, 00153 Rome, Italy
[d] INFN Sezione di Genova, 16146 Genova, Italy
[e] INFN Sezione di Bari, 70126 Bari, Italy
[f] Thomas Jefferson National Accelerator Facility, Newport News, VA, 23606, USA
[g] Argonne National Laboratory, Lemont, IL, 60439, USA
[h] Duquesne University, Pittsburgh, PA, 15282, USA
[i] University of Connecticut, Storrs, CT, 06269, USA
[j] The George Washington University, Washington, DC, 20052, USA
[k] Universidad Técnica Federico Santa María, Casilla 110-V Valparaíso, Chile

ARTICLE INFO

Keywords:
Ring-imaging Cherenkov detectors
PID detectors
Single-photon detection

ABSTRACT

A ring imaging Cherenkov (RICH) detector has been installed in the CLAS12 spectrometer at Jefferson Laboratory (JLab) to provide kaon identification in the momentum range between 3 GeV/c and 8 GeV/c. The detector adopts a hybrid optics solution with aerogel radiator, light planar and spherical mirrors, and highly segmented photon detectors. We report here on the design, construction, and initial performance of the RICH during the commissioning of the detector and the first physics data taking period.

1. Overview

Particle identification (PID) of hadrons in the original baseline design of the Forward Detector of CLAS12 is obtained by combining the information from the High Threshold Cherenkov Counter (HTCC) [1], Low Threshold Cherenkov Counter (LTCC) [2], and Forward Time-of-Flight (FTOF) [3] systems. However, no sufficient separation of kaons from pions and protons can be achieved by using only these detectors in the momentum range relevant for the approved semi-inclusive deep inelastic scattering (SIDIS) physics program, i.e. between 3 GeV/c and 8 GeV/c. Therefore, improved particle identification in this momentum range is achieved by replacing two sectors of the existing LTCC with Ring Imaging Cherenkov (RICH) detectors. The first module of the RICH detector was completed before the start of the physics run, see Fig. 1, while the installation of the second module in the opposite sector is foreseen at the beginning of the CLAS12 operation with polarized targets. This article reports on the design, construction, and initial performance of the first RICH module. The second module will be identical to the first one.

The idea of a RICH detector is based on the fact that when a fast particle crosses a radiator with a velocity β larger than the velocity of the light in that medium, it generates Cherenkov radiation. The light is emitted in a cone with opening angle θ_C given by $\cos(\theta_C) = [\beta n(\lambda)]^{-1}$, where $n(\lambda)$ is the refractive index of the radiator, which may depend on the wavelength λ. Following an expansion volume where the light cone opens up, the photons are detected and the RICH ring can be reconstructed. A precision measurement of the Cherenkov angle provides the determination of the particle velocity and, together with information from the tracking system, it allows its identification. Thus, the capability of identifying the particle types with a known momentum and different velocity is governed by the Cherenkov angle resolution, and it can be effectively parameterized by the separation in units of resolution n_σ between the angle distributions of the various particles.

* Corresponding author.
E-mail address: contalbrigo@fe.infn.it (M. Contalbrigo).

https://doi.org/10.1016/j.nima.2020.163791
Received 19 December 2019; Received in revised form 11 March 2020; Accepted 11 March 2020
Available online 13 March 2020
0168-9002/

Fig. 1. The first module of the CLAS12 RICH installed in Sector 4 of the Hall B Forward Carriage.

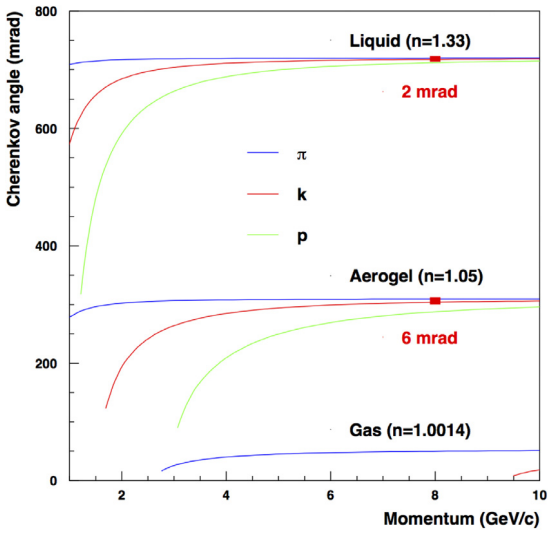

Fig. 2. Cherenkov light opening angle as a function of the momentum for different particles using liquid, gas, or aerogel radiators. The angular separation between kaons and pions at the highest momenta is also indicated.

2. The RICH detector requirements and design

The CLAS12 spectrometer in Hall B [4] is designed to operate with highly polarized beams and nucleon targets at a luminosity of 10^{35} $cm^{-2}s^{-1}$. According to the SIDIS Monte Carlo studies, the kaon production rate is about one order of magnitude lower than the rates of pions and protons in most of the kinematic plane. Thus, successful kaon identification requires a rejection factor from pions around 1:500, i.e. a contamination in the kaon sample of a few percent. This corresponds to 4σ separation. In the momentum range between 3 GeV/c and 8 GeV/c, neither gas nor liquid radiators provide sufficient angular separation to achieve the required pion rejection factor (see Fig. 2) and the only viable solution is the use of silica aerogel as radiator. Aerogel is an amorphous solid network of SiO_2 nanocrystals with a very low macroscopic density and a refractive index in between gases and liquids.

To detect the Cherenkov light emitted in the visible wavelength range, Hamamatsu multi-anode photomultiplier tubes (MaPMTs) were chosen for their high quantum efficiency in the visible and near ultraviolet (UV) regions, their fast response, and the required spatial resolution. Since the RICH detector must fit into the original CLAS12 Forward Carriage, there were several constraints imposed upon its design. Each sector requires a projective geometry, limited depth of 1.2 m, and ~4.5 m^2 entrance windows. Simulation studies favored a hybrid imaging Cherenkov detector design incorporating aerogel radiators, visible light photon detectors, and a focusing mirror system. The focusing mirror system is used to reduce the detection area instrumented by the photon detectors to ~1 m^2 per sector, minimizing costs and influence on the downstream FTOF and Electromagnetic Calorimeter [5] systems. Depending upon the incident particle track polar angle, Cherenkov light is either imaged directly or after one or more reflections and passes through the aerogel. Fig. 3 shows a schematic view of two examples of direct imaging and imaging after multiple reflections. Such a peculiar hybrid-optics design is an innovative solution that has been successfully validated with a test-beam campaign [6].

The RICH detector replaces two sectors of the existing gas Low Threshold Cherenkov detector (LTCC), which is located at a 5-m distance from the beam–target interaction point. The first RICH module was designed while the CLAS12 spectrometer was already under construction and, as a consequence, it had to cover the same large area to match the trapezoidal shape of the LTCC sector. This resulted in several

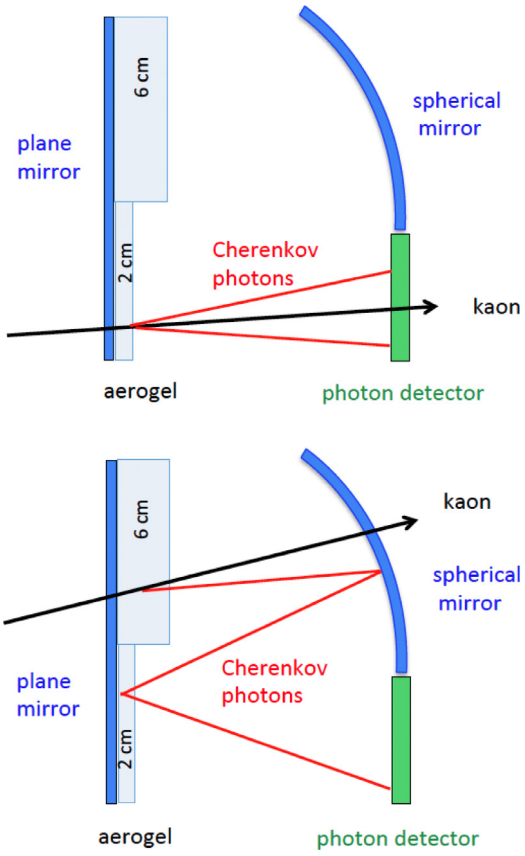

Fig. 3. Examples of CLAS12 RICH imaging: direct detection of the Cherenkov cone produced in the thin aerogel layer (top plot); detection of the Cherenkov cone produced in the thick aerogel layer after multiple reflections and passes through the thin aerogel layer (bottom plot). The plot is not to scale.

challenging requirements for the mechanical structure. The guiding principles are to minimize the material budget inside the acceptance and to limit the impact on the downstream detectors, ensuring at the same time the rigidity of the structure imposed by the optical requirements. Therefore, light materials, in particular carbon fiber, are

chosen for the most of the elements inside the CLAS12 acceptance. For all the parts with large dimensions, the sandwich technique, in which two thin solid skins are glued together on a thick honeycomb core, was also used. This technique indeed combines high stiffness with substantial weight reduction, resulting in a total weight of the detector of about 900 kg, ∼30% lower than the LTCC.

A sketch of the detector is shown in Fig. 4. It is composed of a trapezoidal box (larger base of 4.2 m, smaller base of 0.3 m, height of 3.7 m, and depth of 1.2 m) in which all of the active elements are installed: the wall of aerogel tiles, the mirrors, the photomultiplier tubes (PMTs), and the electronics. The main structural elements of the box are: the two lateral panels made of aluminum sandwich, the top panel made of carbon-fiber sandwich, and the two upper angular elements and the bottom element made of aluminum. Each of the lateral panels supports two planar mirrors, while another planar mirror is installed on the bottom of the box. The box is closed on the front face (with respect to the beam direction) by two entrance panels made of a sandwich of two 1-mm-thick carbon-fiber skins glued on a Nomex honeycomb core. Two planar mirrors with a wall of 2-cm-thick aerogel tiles are installed on the lower entrance panel, while a wall made of two layers of 3-cm-thick aerogel tiles is installed on the upper one. Therefore, the profile of the entrance panels was specifically designed not only to ensure the best light and gas tightness, but also to include stiffening ribs for the installation of the mirrors and the aerogel. The same sandwich structure was used for the electronics panel, located on the bottom part of the backward face of the box. It is composed of a main panel where all of the front-end electronics and the PMTs are installed, and a thin cover. The panel and the cover are screwed together on the mechanical structure, making a very rigid system. Finally, a very light exit panel made of a thin Tedlar sheet glued on an aluminum frame not supporting any active element, closes the back face of the trapezoidal box.

The total material budget of the detector is largely dominated by the electronics panel, which contributes to approximately $0.3X_0$ in the region from the beamline up to about 17°. A sizable contribution comes also from the aerogel (with a maximum contribution of $0.05X_0$ in the polar angles from 17° to 26°), while other active components like the spherical and planar mirrors contribute only $\approx 0.01X_0$ each. The total material budget of the passive elements is estimated to be, on average, below $0.05X_0$.

The mechanical structures and all of the active elements (mirrors, aerogel, electronics, MaPMTs) define the RICH detector. The RICH is attached to the CLAS12 Forward Carriage by means of steel connections, attached to the angular and bottom elements. Detailed Finite Element Analysis (FEA) studies were performed in order to optimize the design of the detector with respect to the maximum deformation allowed by the required accuracy of the optical systems. These studies included optimization of the ratio between the skin and honeycomb thicknesses of the sandwich, and of the total thickness and profile of various stiffening and connection elements. Simulations of the load conditions during the assembly and installation of the detector and in the RICH final position in CLAS12 were also performed together with a seismic analysis.[1] These simulations demonstrated that all stresses produced on the detector elements during the installation are well within the elastic regime, and that the total deformations expected when the RICH is installed in CLAS12 never exceed a few millimeters.

3. The RICH detector components

3.1. The aerogel radiator

The aerogel radiator was produced by the *Budker and Boreskov Institute of Nuclear Physics* (Russia), which was able to fabricate tiles of different shapes and thicknesses, a critical requirement of the complex CLAS12 geometry. A total of 102 tiles with nominal refractive index 1.05, cut into squares 200 × 200 mm^2, as well as pentagonal, trapezoidal, and triangular shapes, were assembled in two sections. The first section, covering the region between the beam pipe and the polar angle of 17.5°, was made of one layer of 2-cm-thick tiles. The second section, covering the polar angles between 17.5° and 26°, was made of two layers of 3-cm-thick tiles, the largest aerogel tiles ever used in Cherenkov imaging applications at this high value of refractive index.

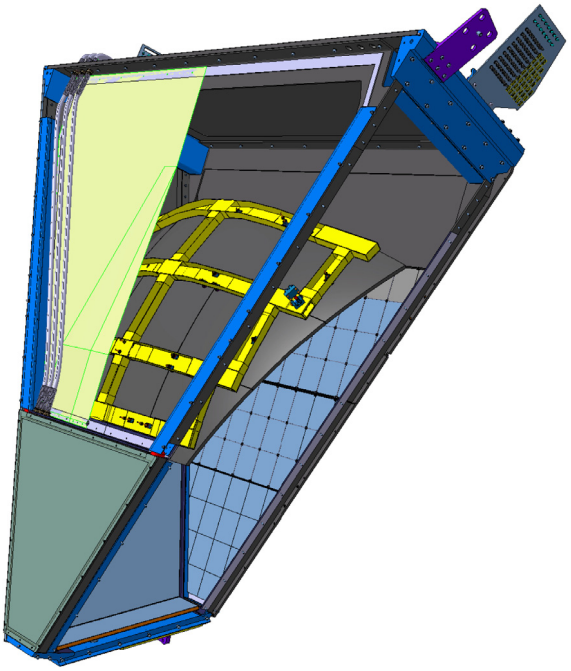

Fig. 4. A schematic drawing of the CLAS12 RICH (rear view) with the internal components highlighted. From left to right, the components of the upper half are exit panel, spherical mirror support and sub-mirrors, double 3-cm-thick aerogel layer, and entrance panel. The components of the lower half are cover, electronics panel — mounting the front-end readout and the MaPMT sensors, 2-cm-thick aerogel layer, front planar mirrors, and entrance panel.

Each tile was tested to determine the geometric and optical parameters [7]. The measured geometric parameters are the side length and thickness, and the planarity of the tile surface. The measured optical parameters include the refractive index at the reference wavelength of 400 nm, and the light transmission as a function of the wavelength. The transparency parameter A_0, the clarity parameter C, and the scattering length L_{scatt} at 400 nm are then extracted from the measured optical properties using the Hunt parameterization [8]. Distributions of the measured values of the refractive index, transparency A_0 (in percent), and scattering length L_{scatt} for the square 2 cm tiles are shown in Fig. 5. The average values obtained over all of the 2 cm tiles are L_{scatt} = 50.5 mm, A_0 = 0.975, and C = 0.00512 μm^4/cm. The 3 cm tiles feature similar optical quality [7]. From these measurements, the expected photon yield for $\beta = 1$ particles is estimated to be about 19 photoelectrons (p.e.) in the 2 cm sector and about 25 in the 6 cm (3 cm + 3 cm) sector.

3.2. The mirror system

The mirror system, composed of planar and spherical mirrors, was designed to minimize the photon loss and to direct as much of the Cherenkov radiation as possible toward the photodetectors. Simulations were performed to optimize the segmentation, the position, and the radius of curvature of these mirrors, and to define the specifications of the optical performance. A drawing of the system is shown in Fig. 6.

[1] According to US regulations, seismic analyses are performed by increasing the expected weight load by 10%.

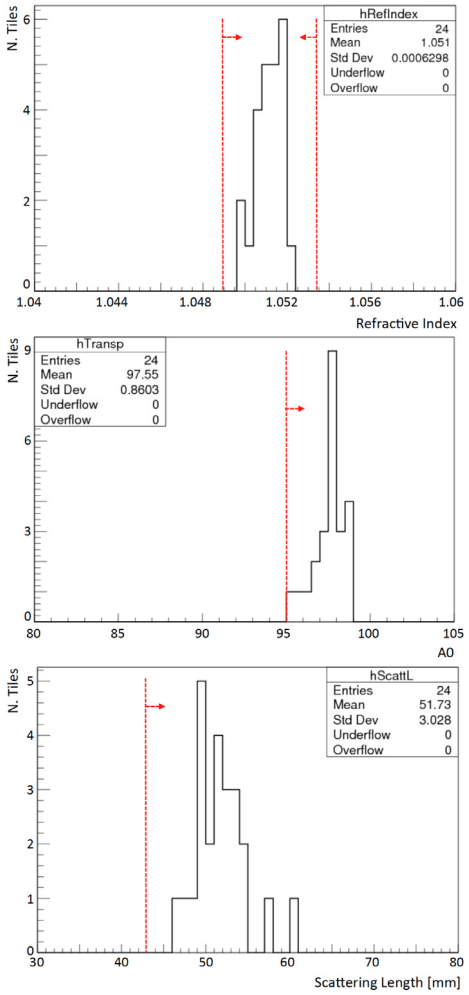

Fig. 5. Distributions of the measured refractive index (top plot), transparency A_0 (in percent, central plot), and scattering length L_{scatt} (bottom plot) for the square 2 cm tiles. The red dashed lines indicate the specification limits.

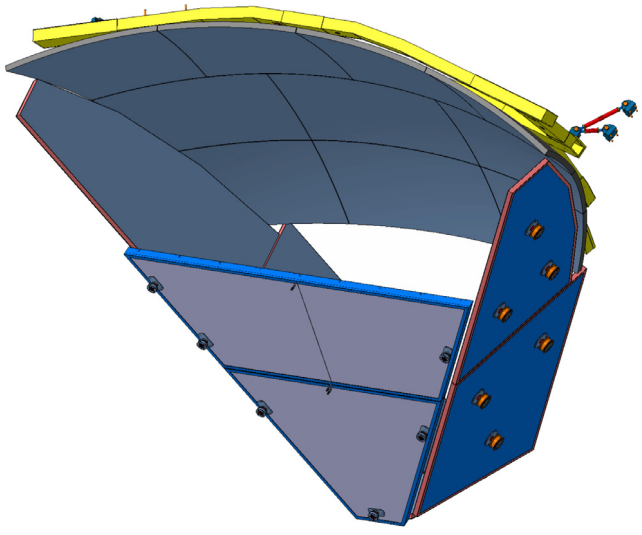

Fig. 6. Drawing of the CLAS12 RICH mirror system with their mounting joints (front view). The 10 sub-mirrors of the spherical mirror face the two front planar mirrors. An array of planar mirrors, two on each side and one (not visible) on the bottom, completes the light-containment system.

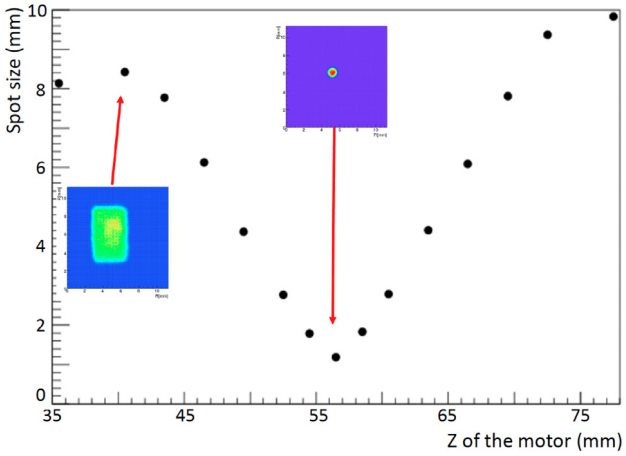

Fig. 7. D_0 as function of the distance between the mirror and the camera for one of the spherical sub-mirrors. The two inserts show the shape of the reflected spot at the beginning of the distance scan and at the minimum.

3.2.1. The spherical mirrors

The spherical mirror system, installed inside the RICH box in front of the exit panel, has a total surface of about 3.6 m^2, a radius of curvature $R = 2.7$ m, and is segmented into 10 sub-mirrors. They were produced by the *Composite Mirror Applications* company [9], and are made of two layers of carbon fiber glued on a honeycomb core of small carbon-fiber cylinders. The areal weight of these mirrors is less than 5 kg/m^2, with an improvement of about 20% with respect to the mirrors produced by the same company for the LHCb experiment [10]. Each mirror is positioned on a light carbon frame by means of three special joints equipped with a spring and a precision screw that allowed their relative alignment. The frame is then attached to the mechanical structure by means of three similar joints that allow the alignment of the full mirror system with respect to the other active elements of the detector.

The accuracy of the spherical surface of the sub-mirrors was quantified by means of a so-called spot size measurement, in which each mirror was illuminated with a point-like light source and the size of the reflected spot was measured by a XIMEA camera with a 1-cm-wide CMOS sensor. The size of the spot is quantified by D_0, which is defined as the minimum diameter containing 90% of the total reflected light, and is related to the angular resolution of the reflected photons by the relation

$$\sigma_\theta = \frac{D_0}{8R}, \tag{1}$$

where the angular dispersion is derived from the 2σ-spot radius $D_0/2$ divided by the traveled distance $2R$ [11]. The smaller D_0 is, the closer the mirror surface is to a perfect sphere. The measurements also allow for the extraction of the radius of curvature, which corresponds to the distance between the camera and the mirror where the spot size is minimal. The results of a typical measurement of one sub-mirror are shown in Fig. 7, where D_0 as a function of the distance and the shape of the spot at the beginning of the distance scan and at the minimum are shown. All of the sub-mirrors exhibit a D_0 smaller than 1.5 mm, which means σ_θ significantly below 1 mrad, and a variation in the measured radii below 0.5%. All of these numbers are well within the specifications.

The sub-mirrors were coated with a reflecting layer by *Evaporated Coatings Inc* [12]. The quality of this coating was verified by measuring the reflectivity on several surface spots in the wavelength range from 300 to 650 nm. For all of the sub-mirrors, we obtained on average a reflectivity between 88% and 90%, relatively flat over the whole wavelength range.

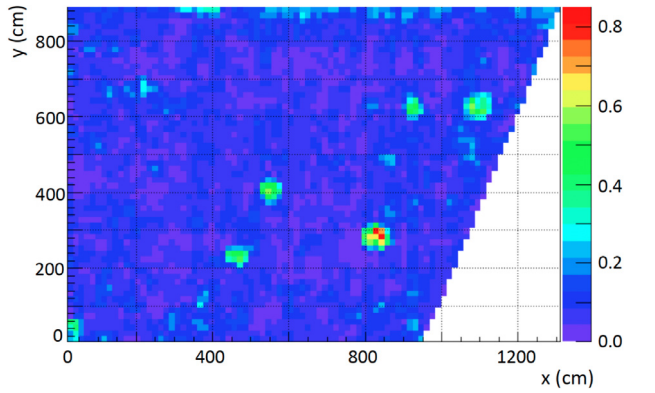

Fig. 8. Profile of the local slope (indicated by the color scale in mrad) of the surface of one of the lateral planar mirror measured with a CMM. (For interpretation of the references to color in this figure legend, the reader is referred to the web version of this article.)

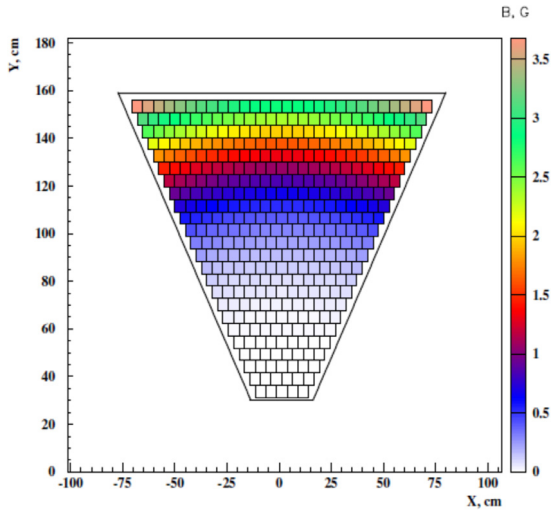

Fig. 9. Calculated map of the torus fringe field strength (in Gauss) in the RICH photodetector area. (For interpretation of the references to color in this figure legend, the reader is referred to the web version of this article.)

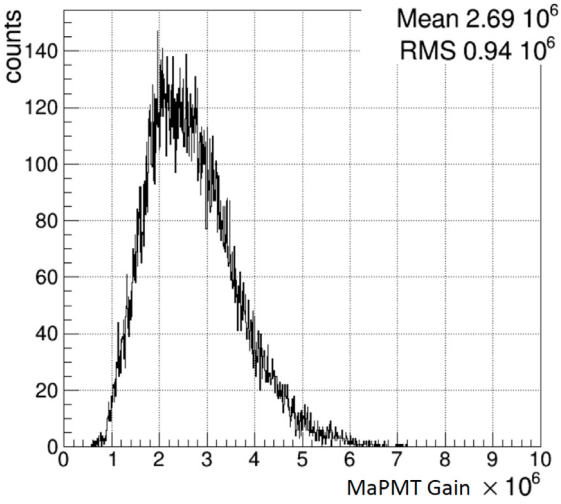

Fig. 10. Distribution of the data-sheet gains of the 25k RICH MaPMT channels.

3.2.2. The planar mirrors

The planar mirror system is composed of 7 mirrors: two installed on each of the lateral panels, two on the front panel, and one on the bottom, for a total surface area of about 6.5 m^2. These mirrors were produced by the *Media Lario* company [13] and are made of two thin layers of glass glued on an aluminum honeycomb core. This is a standard technique widely used in telescopes for astrophysics studies but used for the first time in nuclear physics experiments, and allows for the production of mirrors as light as the carbon fiber ones but at much lower cost. Being in the acceptance of the detector, the front mirrors use very thin (0.7 mm) glass layers, allowing a reduction of the material budget down to about $0.01X_0$, while for the lateral and the bottom mirrors, thicker (1.6 mm) glass layers were used.

The planarity of the mirror was measured with a Coordinate Measuring Machine (CMM). Typically, the measured accuracy of the surface was a few microns RMS. To better quantify the quality of the surface, the local slope profile was reconstructed from the spatial profile, as shown for one of the lateral mirrors in Fig. 8, where we see only a few spots with non-zero slope over a largely flat surface. All of the mirrors satisfy the requirement that only a few percent of the total surface should exceed a local slope of 0.3 mrad.

The characterization of the planar mirrors was completed by measuring the reflectivity in a few random spots of the surface in the wavelength range from 300 to 650 nm. The measurements showed a maximum reflectivity of approximately 95% at 400 nm and a reflectivity higher than 90% in the whole range.

3.3. The photon detector

Thanks to the use of mirrors, the active area is minimized to about 1 m^2. The instrumented area is optimized to cover the most effective region close to the beam pipe, which is where the density of particles per unit area is the highest, the particle momenta are to a large extent above the FTOF working range, and the hadron identification requires the best RICH performance.

3.3.1. The photosensor

Due to the imaging aspects of the RICH, there are several requirements that the photon sensor has to fulfill: it has to efficiently detect single photoelectron (SPE) level signals, it must be sensitive in the visible light wavelengths (due to the aerogel radiator material), it must have the spatial resolution required to achieve the design angular resolution, and it has to provide an active area with minimal dead space. In addition, it has to be insensitive to the low torus fringe field where the RICH readout is located, which is estimated to be no more than 3.5 G, see Fig. 9. The Hamamatsu flat-panel H8500 MaPMT [14] with an 8 × 8 array of 6 × 6 mm^2 pixels over a compact active area of 5 × 5 cm^2 and with high packing fractions (89%), was initially selected as a good candidate. Despite not advertised as the optimal choice in the SPE regime, such MaPMTs showed adequate performance in several laboratory tests [15] and beam tests [16]. Just after the RICH construction startup, a novel Hamamatsu H12700 MaPMT became available, with the same layout as the H8500 MaPMT, but an optimized dynode structure for single photon detection [17].

Of the 391 MaPMTs that the CLAS12 RICH employs, 80 are of the H8500 type and the rest are of the H12700 type. This results in a total of 25024 individual pixels, covering the ~1 m^2 trapezoidal active area of the first RICH module. The production specifications included requirements on the minimum gain of 1×10^6 and a maximum total dark current of 5 nA. Both were fully achieved. Fig. 10 shows the distribution of the pixel gains, which has an average value of 2.7×10^6, corresponding to about 430 fC generated charge per SPE.

3.3.2. The readout electronics

The RICH front-end electronics are designed to ensure 100% efficiency at 1/3 of the average photoelectron signal level, 1 to 4 gain spread compensation, time resolution of the order of 1 ns to distinguish

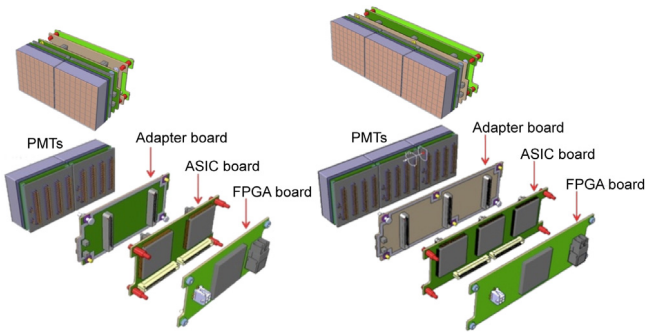

Fig. 11. The CLAS12 RICH readout unit design (see text for details).

direct from reflected photon hits, and a trigger rate up to 20 kHz with 8 μs trigger latency and negligible dead time [18].

The front-end electronics are organized into compact units (called tiles, see Fig. 11) mechanically designed to fit the MaPMT dimensions, each serving two or three MaPMTs, thus allowing the tessellation of large surfaces with minimum dead space and material budget. Each readout unit comprises three boards with complementary functions.

A feed-through adapter board provides the electrical connectivity of the sensors with the external readout system, while preserving the adequate light and gas tightness of the inner detector volume when mounted on the RICH carbon-fiber supporting panel. It also distributes the sensor bias voltage (with -1000 V as the nominal value).

The signal processing board is based on the MAROC3 chip [19], a 64-channel microcircuit dedicated to MaPMT pulse processing. Each channel comprises a low impedance adjustable gain preamplifier followed by two highly configurable shaping sections with independent processing. The first section embeds a slow shaper and a sample-and-hold structure to allow linear charge measurements up to 5 pC. Requiring short trigger delays and multiplexed access, this section can be used as a RICH calibration tool. The second section features a fast shaper and an adjustable threshold discriminator to produce, for each input signal, a start and stop logic pulse. A constant-threshold binary readout requires good stability of the baseline (pedestal) and definition of the working point (gain and threshold). During the board production, quality assurance tests confirmed the excellent sensitivity of the logic readout, able to discriminate signals down to a few percent of a single photoelectron discharge, as will be extensively discussed in Section 4.2.

The third stage of the readout is made of the FPGA boards, hosting a Xilinx7 FPGA chip, responsible for configuring and reading the front-end MAROC3, distributing the trigger, and interfacing with the data acquisition system [20] via optical link. The FPGA provides a TDC functionality with a 1 ns time stamp for both start and stop times. The start time is used for timing purposes, while the difference between the stop and start times, the so-called Time-Over-Threshold (ToT), provides a non-linear estimate of the amplitude of the input signal and is used for the time-walk correction, see Section 5.2. Finally, the FPGAs also embed a scaler readout that is used as a calibration and monitoring tool.

3.3.3. MaPMT characterization

The characterization of hundreds of MaPMTs is a challenging problem. In order to test them efficiently within a reasonable time frame, a fully automated test stand was built to evaluate 6 MaPMTs at once. The test stand consists of a 470 nm diode laser system, 2 long-travel motorized stands to drive a laser fiber in two-dimensional space for individual pixel illumination, and a motorized neutral-density filter system. The laser light is directed through the fiber and attenuated to the single-photon level using neutral-density filters to mimic the conditions of the RICH detector. The motors are remotely controlled to move the focused laser 1 mm beam spot across the entire surface of

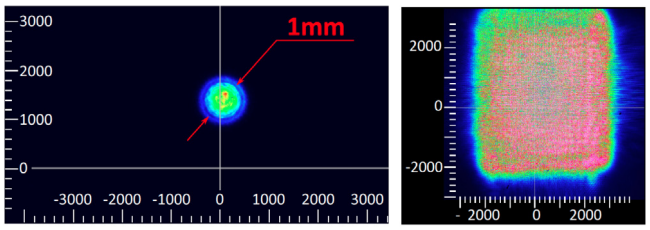

(a) Focused laser beam. (b) Square pattern.

Fig. 12. The MaPMT test stand laser output options. The images are taken at an arbitrary distance from the source, the scale is in micron.

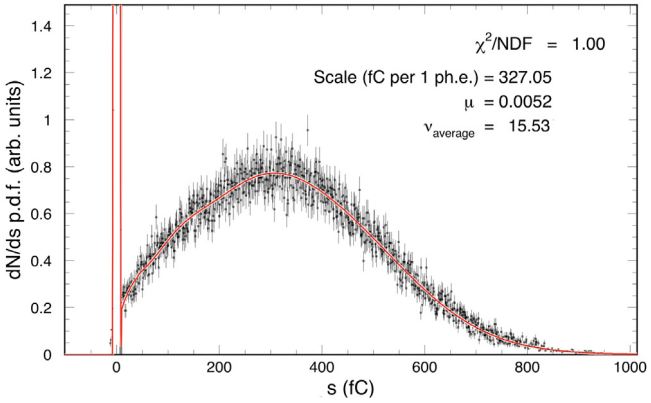

Fig. 13. Sampled H8500 MaPMT single photoelectron spectrum from one of the pixels at 1000 V with a low-intensity laser light source. The fit function (see details in Ref. [21]) is shown as a solid line. The relevant parameters (see text) are $\mu = 0.0052$, $\nu_{average} = 15.53$, and $scale = 327$ fC. This corresponds to a MaPMT gain of 2.0×10^6.

the MaPMT entrance window and illuminate one by one the 64 pixels individually (see Fig. 12(a)). Alternatively, one can illuminate the whole surface of the MaPMT photocathode at once using an Engineered Diffuser to produce a square pattern with a non-Gaussian intensity distribution (see Fig. 12(b)). The latter configuration was used for the massive characterization of the RICH MaPMTs, bringing routine workloads to a minimum. The evaluation of 6 MaPMTs (corresponding to 384 individual channels) at 4 different high voltages and 6 different light intensities was completed in 6 h with less than 15 min of human intervention.

The characteristics of the SPE spectrum were studied using the charge measurement functionality of the slow shaper of the MAROC3 chip. A new computational model [21] for the description of the PMT response functions of both the H8500 and H12700 MaPMTs was developed. Important features of the model include the ability to approximate the true SPE spectra from different PMTs with a variety of parameterized spectral shapes. The predictive power of the model was tested by demonstrating that the SPE spectral parameters, obtained in the measurements, well describe the amplitude distributions of the same photodetector measured at different levels of illumination. Thus, the model allowed us to extract the characteristic parameters of the devices independently of the test measurement conditions.

The SPE spectrum is extracted by fitting the signal amplitude distribution with the model function measured as shown in Fig. 13 for the H8500 MaPMT and in Fig. 14 for the H12700. The x-axis is calibrated in terms of charge measured by the MAROC3 chip. To approximate the performance of the first amplification cascade of the MaPMTs, the probability function was introduced in the model as a trinomial sum of three Poissonian distributions with different average secondary multiplicities and the corresponding three relative probabilities for every photoelectron to generate secondary electrons (see Ref. [21] for more details). In each fit, the parameter μ corresponds to the average

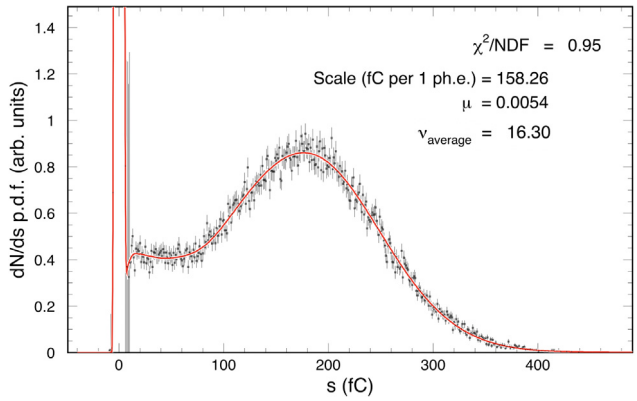

Fig. 14. Sampled H12700 MaPMT single photoelectron spectrum from one of the pixels at 1000 V with a low-intensity laser light source. The fit function (see details in Ref. [21]) is shown as a solid line. The relevant parameters (see text) are $\mu = 0.0054$, $\nu_{average} = 16.3$, and $scale = 158.26$ fC. This corresponds to a MaPMT gain of 0.98×10^6.

number of photoelectrons generated at the photocathode by each laser pulse, $\nu_{average}$ is the average number of secondary electrons generated at the first dynode, and $scale$ is the average anode charge collected from one photoelectron.

In the single-photoelectron amplitude spectra shown in Figs. 13 and 14, the normally significant contributions of the cross-talk signals, caused by the photoelectron amplification cascades in the neighboring PMT channels, have been removed by using the filter masks covering the neighbors, and leaving open only the pixel studied. The detailed discussion of the method will be given in [22]. The data showed that the H12700 has, on average, a 10% better efficiency than the H8500, likely due to the improved photocathode performance and collection efficiency. An example of the results for one MaPMT is shown in Fig. 15. The parameter $scale$ (top plot), characterizing the amplification (dynode) system, is virtually independent of the light radiation level, while strongly dependent on the high voltage setting, the exact behavior one would expect from the characteristics of the internal dynode system of a MaPMT. The central plot shows the average number of photoelectrons μ measured with different optical filters. It indicates that all of the channels respond in the same way as the light intensity increases. This parameter is practically independent of the applied voltage, as expected. The parameter $\nu_{average}$ (bottom plot) that is related to the first dynode performance, has a weak dependence on the bias voltage and is independent of the level of light radiation as well.

The results of the characterization have been stored in the CLAS calibration database and are available for use in the Monte Carlo simulations. The extracted gain values have been used to perform the equalization of all 25024 readout channels.

The SPE spectra allow for the study of the SPE response dependence on the working parameters, i.e. MaPMT bias voltage, MAROC pre-amplification gain, and discriminator threshold[2] using the binary readout line. Data indicated that the efficiency reaches a plateau over a wide range of working parameter values [18]. The plateau corresponds to the region where all of the MaPMT discharges are digitized and the efficiency ultimately depends on the quality of the photocathode. The plateau is a consequence of the saturated mode employed in the MAROC binary readout and allows a flexible definition of the working point, a crucial feature when dealing with a large number of channels in the challenging single-photon regime.

[2] The programmed threshold levels are expressed in Digital-to-Analog Converter (DAC) units, 1 DAC unit corresponds to about 1 mV.

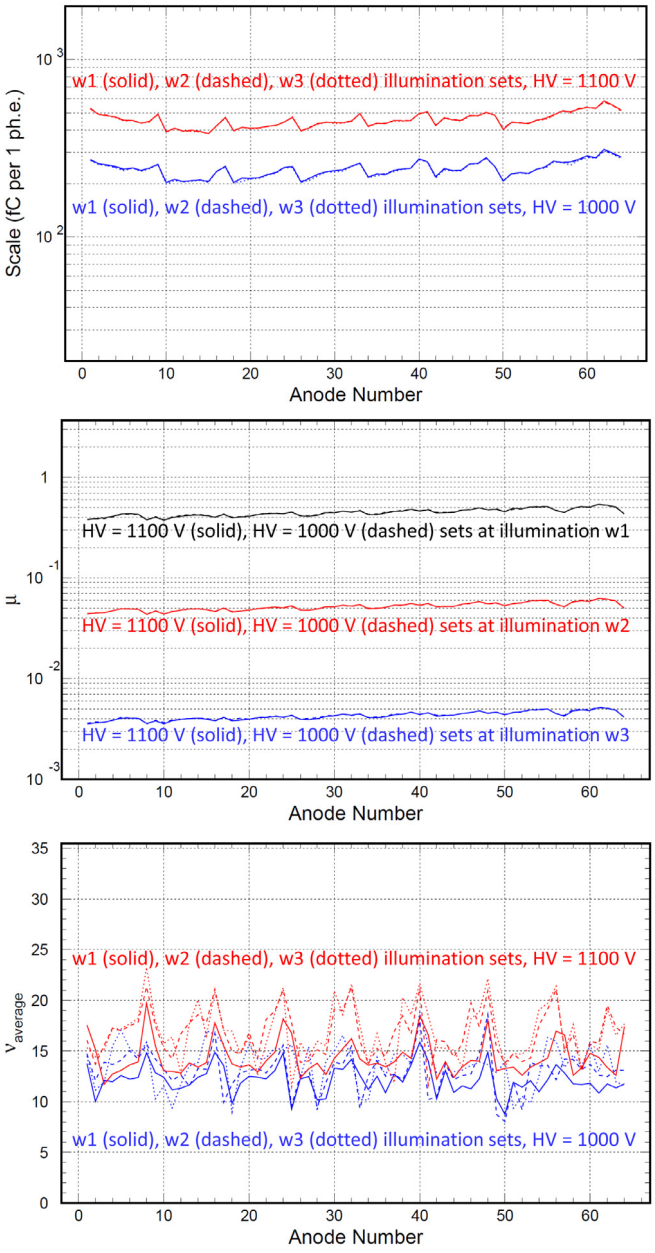

Fig. 15. Distributions of fit parameters measured at 2 different high voltages (1000 V and 1100 V) and 3 different light intensities (w1:w2:w3 ~ 100:10:1) for 64 pixels of one MaPMT: the parameter $scale$ characterizing the dynode amplification system (top), the average number of photoelectrons μ (center), and the first dynode amplification ν (bottom).

3.4. The detector services

The CLAS12 RICH requires various services, namely power, cooling, and gas purge whose number of lines has to be minimized and installed outside of the CLAS12 acceptance. A continuous nitrogen flow, supplied by the Hall B gas distribution system, is provided in order to keep the relative humidity inside the RICH vessel at a few percent level. The flow is set to about 40 liters per minute to ensure a complete inner volume exchange every few hours. A backup system has been realized by a stack of nitrogen bottles to allow for up to 3 days of gas flow in case of failure of the primary distribution system.

The electronics power is controlled by a CAEN SY4527 power supply with five 8-channel A2518 low voltage (LV) boards and five 32-channel A1536 high voltage (HV) boards. Each LV channel powers 4 readout

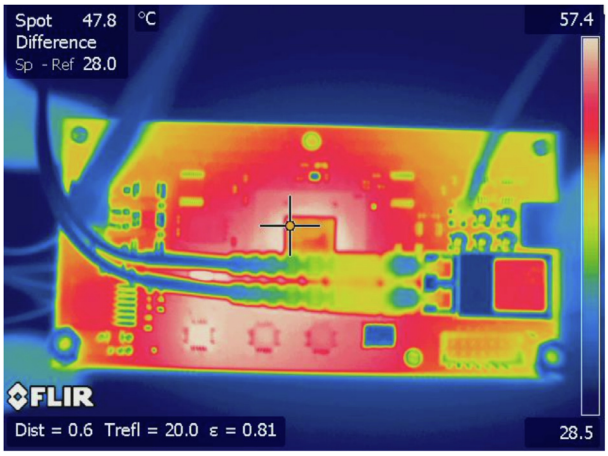

Fig. 16. The CLAS12 RICH readout unit as imaged by a thermo-camera. The hottest spots are the FPGA chip in the center and the optical transceiver on the right. (For interpretation of the references to color in this figure legend, the reader is referred to the web version of this article.)

units, while each HV channel drives the MaPMTs grouped in one readout unit. The electronics readout is connected to the back-end by three MTP trunks of 2.5 Gbps optical fibers. One trunk groups several multi-core fibers, each of them connecting one of the eight ports in the VME/SSP [20] back-end module to four FPGA boards.

The readout electronics dissipates about 3.5 W per unit, mainly due to the FPGA chip and the optical transceiver, as shown by the thermo-camera image in Fig. 16. The total heat load, at the level of 500 W, is removed by a forced air flow. Since the electronics panel is not fully sealed due to the numerous holes for the readout and HV connectors, there is a diffusive exchange in the RICH vessel between the nitrogen gas used to keep the aerogel dry and the air in the electronics panel. As a consequence, dry and clean air is required to cool down the electronics. This is achieved with an Altas Copco multi-core oil-free rotary scroll air compressor. The compressor fills a tank at 8 atm pressure, from where the cooling air is filtered and circulated toward two distributors located at the sides of the electronics panel and outside the acceptance. These are made of stainless-steel tubes with several nozzles to direct the cooling air supersonic flow along the board surface. The exhaust is made of six corrugated tubes that run in the back of the RICH module behind the spherical mirror.

4. The RICH detector installation and commissioning

4.1. RICH assembly

The assembly of the RICH detector was performed in a clean room and each element was installed after the completion of the relative characterization tests. The trapezoidal RICH vessel was attached to a large aluminum structure with a pivot to rotate the detector from the vertical to the horizontal position, as required by the various assembly phases.

The ten spherical sub-mirrors were mounted on a common frame inside the RICH vessel. To minimize the material budget, the frame is composed by a net of 1.5-mm-thick carbon-fiber U-profiles. Each element (frame and sub-mirrors) has three mounting points designed to allow precise alignment. The relative alignment of the sub-mirrors was performed with the same setup used to determine their surface accuracy. The full spherical mirror was illuminated by a point-like source and the position of each sub-mirror was adjusted until the ten spot images converged into the nominal center of curvature. In Fig. 17, the reflected images before the alignment (when each sub-mirror produces a spot at a different location) and after the alignment

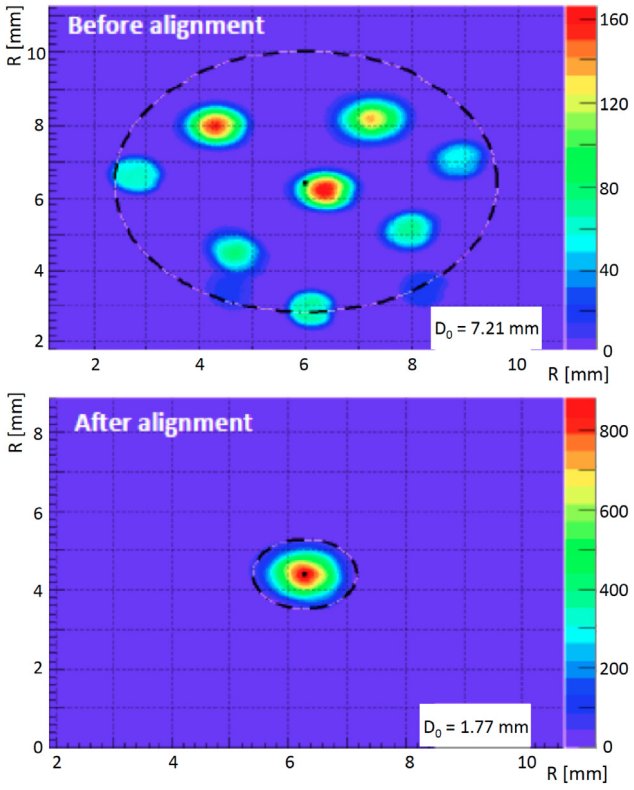

Fig. 17. Reflected spot by the whole spherical mirror system: before the alignment (top plot), all sub-mirrors image the light source in different locations; after the alignment (bottom plot), all images overlap in the same position. The spot brightness depends on how close the sub-mirror center is to the sensor position. (For interpretation of the references to color in this figure legend, the reader is referred to the web version of this article.)

(when all the spots overlap within a few mm) are shown. The quality of the result is also visible in Fig. 18, where the spherical mirror system before (left) and after (right) the alignment is shown.

The lateral and bottom planar mirrors were attached to the RICH trapezoidal vessel structure by means of joints that allow for a precise alignment. The two front mirrors were mounted on the lower front panel made of carbon fiber. The relative position of the mirrors was aligned with respect to the RICH vessel at the level of about 0.5 mrad by using a faro-arm. The fully installed mirror system as seen from the entrance panel is shown in Fig. 19.

The RICH photon detectors and readout electronics were installed on the electronics panel using an independent aluminum support structure to enable easy access and to allow rotations during the functionality tests. The PMTs with higher gain were placed closer to the beam pipe, where better detection performance is required. As the MaPMT in one readout unit share the same HV bias, they were selected to be of similar gain and of the same type (H8500 or H12700). The fully equipped electronics panel is shown in Fig. 20 from the MaPMT side and in Fig. 21 from the readout electronics side.

After the electronics panel assembly was completed, particular care was devoted to minimize and stabilize the pedestal width values. The measured pedestal RMS was initially at the level of few DAC units, with relatively large variations not only from MaPMT to MaPMT but also among the channels of a single MaPMT, as shown in the top plot of Fig. 22. As the readout uses a single threshold value per chip (or MaPMT), the channel-by-channel variation may effect the single channel efficiency in a way that would be complicated to correct for. Therefore, a grounding grid was realized by connecting all of the boards to the detector chassis with a copper wire. In this way, all of the

Fig. 18. The spherical mirror before (top plot) and after (bottom plot) alignment. As a result of the alignment, the image appears continuous along the whole mirror surface.

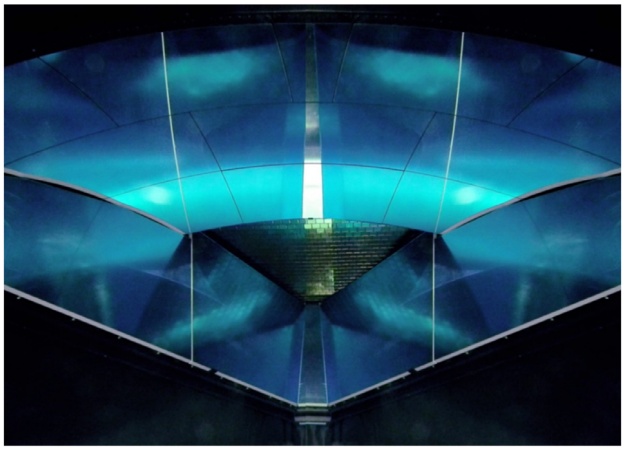

Fig. 19. The mirror system as it is seen from the RICH entrance panel. Clockwise from the top, the ten spherical sub-mirrors, the two right lateral mirrors, the bottom mirror, and the two left lateral mirrors are visible. At the center, the MaPMT array is also visible.

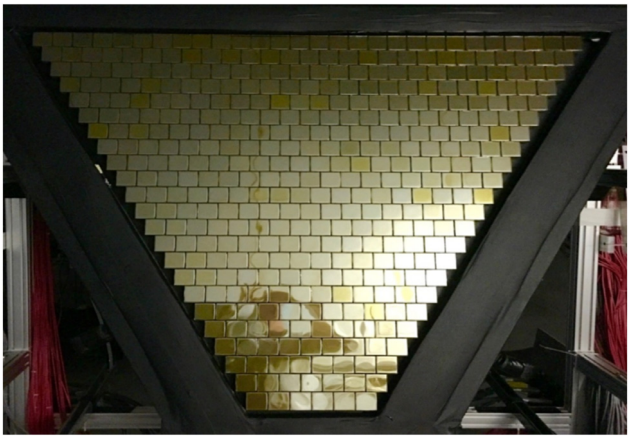

Fig. 20. The fully assembled plane of MaPMTs.

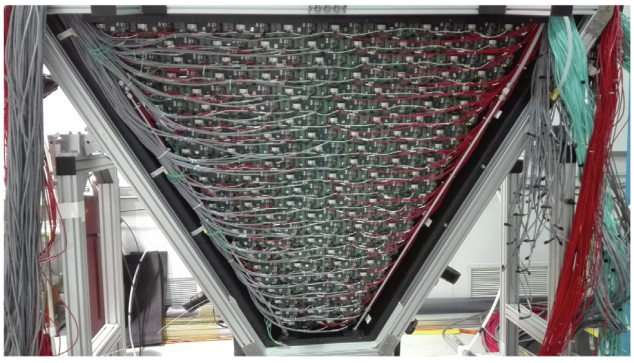

Fig. 21. The fully assembled and cabled front-end electronics. Visible are the gray 20 AWG LV cables, the red HTC-50-1-1 HV cables, and the cyan MTP optical fibers. (For interpretation of the references to color in this figure legend, the reader is referred to the web version of this article.)

components of the readout system, powered by the floating 5 V low-voltage lines, were properly referred to the same ground. This reduced the typical pedestal RMS down to about 1 DAC unit, a level comparable with the test bench results, as shown in the bottom plot of Fig. 22.

Several tests were performed using cosmic rays at various stages of the electronics assembly. In the absence of a precise measure of the cosmic particle momentum, it was not possible to perform any study of the Cherenkov angle resolution. Nevertheless, cosmic runs allowed for the validation of the translation tables relating the electronics channels to the pixel positions, the development of the ring reconstruction software, the verification of the stability of the system, and the testing of the performance of the power supplies, cooling, readout, slow controls, and interlock services. After all planned tests were completed, the complete readout system was eventually transferred into the mechanical structure.

The aerogel was the last element installed, being the most sensitive to the external conditions. For this reason, before its assembly, a test to verify the gas-tightness of the RICH vessel, temporarily completed with all of the closing panels, was performed. Each aerogel tile was inspected and mounted in a pre-selected location of the supporting structure, namely the front mirrors for the 2-cm tiles and the upper front panel for the 3-cm tiles. The location of each tile was determined in order to concentrate the tiles with the higher expected photon yield at forward polar angles where the particle identification requirements are most demanding. In addition, tiles with close optical properties were coupled in the same location of the double 3-cm layer. The tiles were secured in place by a net of nylon wires that ran along the edges and, on the side, by plastic bumpers covered by a thin foam layer to avoid damage to the aerogel. The tiles were also optically isolated from each other by

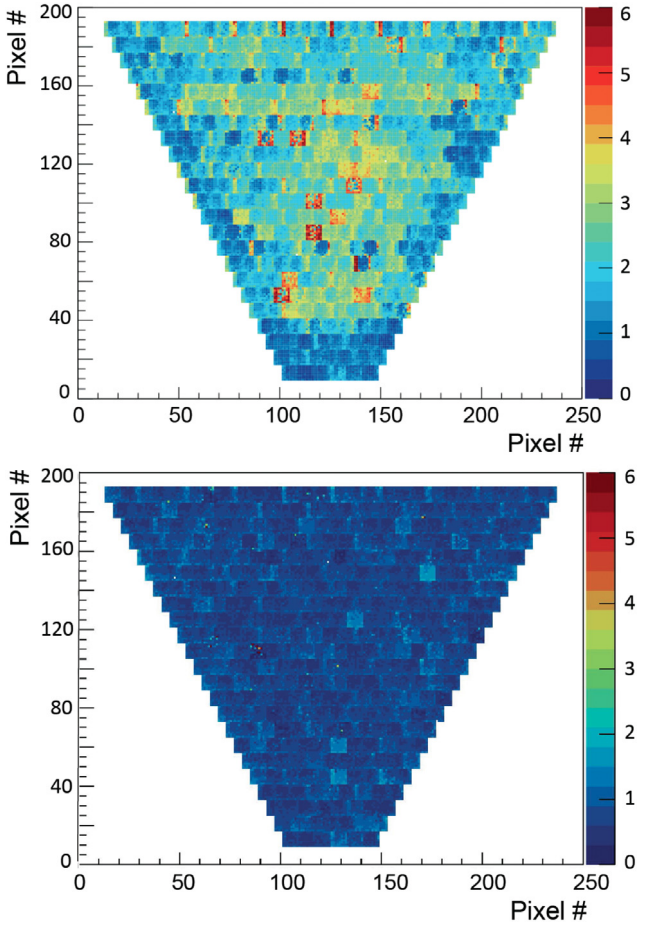

Fig. 22. Map of the pedestal RMS values before (top) and after (bottom) the realization of a grounding grid connecting all of the electronics units to the RICH chassis to provide a common ground reference for the floating power lines. (For interpretation of the references to color in this figure legend, the reader is referred to the web version of this article.)

using a thin layer of foam stretched around each tile. In fact, photons produced in one tile and propagating through an adjacent tile undergo surface effects that generally degrade the angular resolution. The foam is instrumental to avoid sharp edge contacts between the blocks that might originate cracks in the aerogel material. In addition, the foam net bonds the tiles together in forming a sole and stable layer. Fig. 23 shows the front planar mirror system with the aerogel tiles fully installed.

During the assembly, the aerogel panels were maintained in a low-humidity atmosphere (around 20% relative humidity) to prevent moisture absorption. Once the assembly of all tiles was completed, the panels were quickly installed on the RICH vessel, the detector was sealed with all of the closing panels and a flow of purged nitrogen was started to minimize the exposure to the external environment conditions.

Once the detector was sealed and before the transportation to the experimental hall, its functional parameters were tested for several weeks in the assembly room. The tests included the two gas systems serving the RICH: the nitrogen system that must keep the internal humidity at the few percent level to preserve the aerogel optical performance and the air-cooling system of the readout electronics.

4.2. RICH commissioning

The RICH detector was installed in the CLAS12 spectrometer at the beginning of January 2018, in time with the start of the first data taking in Hall B. In preparation for the data taking, a number of tests were routinely performed without and with beam to establish the running conditions and to verify the stability of the response.

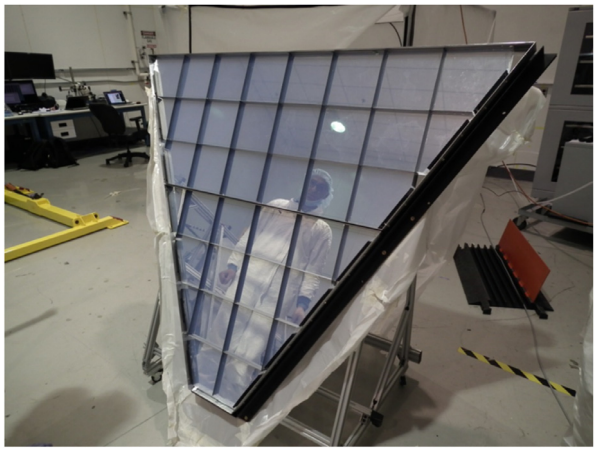

Fig. 23. The 2-cm-thick section of the aerogel mounted on the two RICH front mirrors. Visible are the external aluminum frame and the black foam net that optically and mechanically isolates each tile from the others.

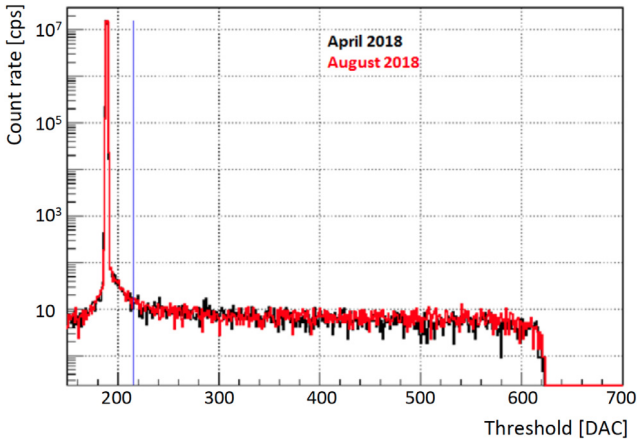

Fig. 24. Example of a SPE spectrum from the dark rate measurement of one readout channel as a function of the threshold value. The two histograms were recorded in April and August 2018. The blue line indicates the threshold setting. (For interpretation of the references to color in this figure legend, the reader is referred to the web version of this article.)

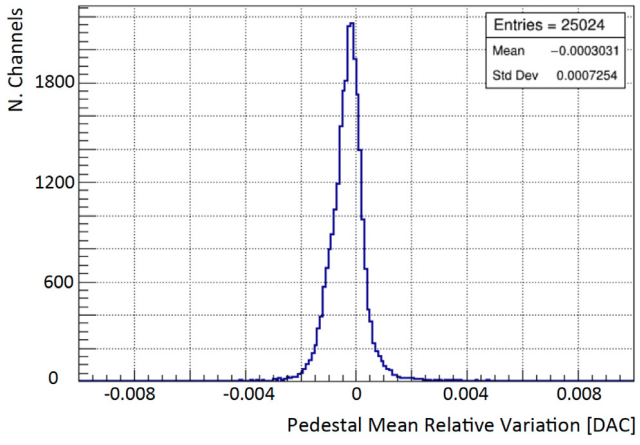

Fig. 25. Relative variation of the mean pedestal position of the 25024 readout channels between April and August 2018.

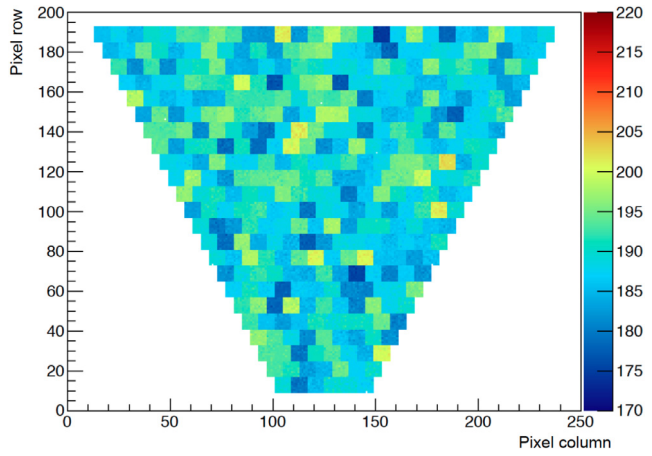

Fig. 26. Map of the mean pedestal position in DAC units (color scale). (For interpretation of the references to color in this figure legend, the reader is referred to the web version of this article.)

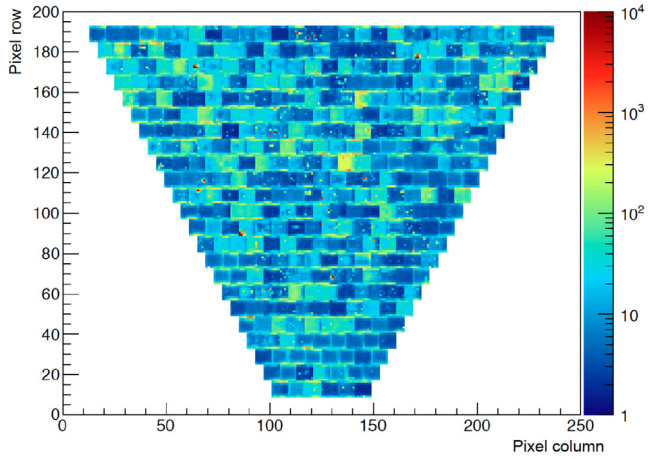

Fig. 27. Map of the average dark count rate in the plateau region of threshold values (color scale). (For interpretation of the references to color in this figure legend, the reader is referred to the web version of this article.)

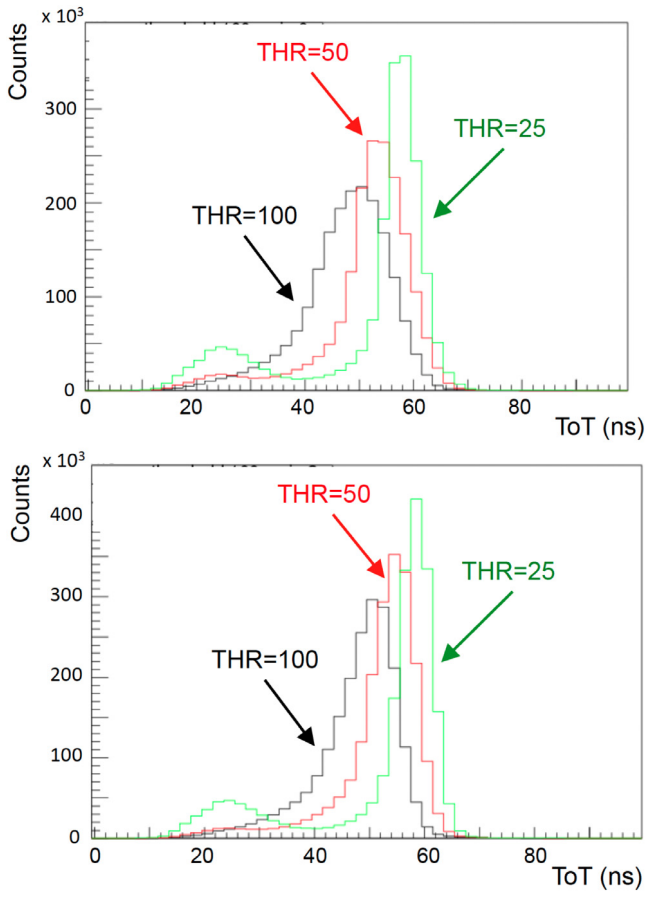

Fig. 28. Time-over-Threshold (ToT) distributions of the RICH channels at three typical values of threshold (25, 50, and 100 DAC) without (top) and with (bottom) gain equalization. The saturated SPE signals generally yield ToT durations greater than 40 ns. When lowering the threshold weaker cross-talk signals are also recorded with ToT durations around 25 ns.
Source: Figure taken from Ref. [18].

The basic tool to monitor the RICH front-end electronics is provided by the measurement of the MaPMT dark noise counting rate. The number of counts above a programmed threshold is recorded for a time period on the order of a second. A fine scan of the threshold value allows for the reconstruction of the full SPE spectrum for each of the 25k channels. An example of one SPE spectrum is shown in Fig. 24. The main features of the data are: *(a)* a very narrow pedestal where the threshold equals the analog baseline, *(b)* a region close to the pedestal where the rate smoothly decreases as the threshold increases (corresponding to the almost linear regime of the MAROC), and *(c)* a large plateau of the saturation regime, where the count rate is basically insensitive to the threshold setting almost up to the edge of the SPE region. The plateau is a crucial feature of the front-end electronics, because it allows a flexible definition of the working point without the need for extreme precision in the channel equalization. Counts at threshold values below the pedestal are due to the bipolar shaped signal. The spectra allow for the channel-by-channel extraction of the pedestal position and width, the dark count rate in the plateau region, and the amplitude of the SPE region. The black and red histograms in Fig. 24, taken in April and August 2018, respectively, demonstrate the stability of the readout system over several months of running. Moreover, in Fig. 25, the relative variation of the mean pedestal position in the same interval of time is shown. On average, the pedestals are stable at the level of 10^{-3}.

The pedestal level is different for each readout channel, but it is quite uniform within one MAROC chip, as can be seen from the map shown in Fig. 26. This result guarantees the effectiveness of the common threshold.

The average count rate in the plateau region provides a measurement of the dark count rate of the channel, as shown in the map of Fig. 27. The typical dark count rate is a few tens of Hz, with more than 99% of the channels below 100 Hz and only few channels above 10 kHz. It is also found that the highest dark count rates in the MaPMTs are located in the first and last row of pixels. Although measured with a completely different setup, these results are in good agreement with the values quoted in the Hamamatsu data sheets.

The MAROC preamplifier equalization gains are determined using the characterization measurements described in Section 3.3.3 by tuning the average MaPMT+MAROC gain to 2.7×10^6 in all channels. The equalization gains range from about 0.5 to 3, with an average value of 1.2. The effect of the channel-by-channel signal equalization was verified during the engineering run by taking data at various thresholds for different MAROC gain configurations. Fig. 28 shows the ToT distribution for three typical values of the threshold, on the top for all channels without amplification (nominal MAROC gain of 1) and on the bottom after equalization. After equalization, the ToT distribution of saturated SPE signals is narrower than with unitary gains. With typical ToT values larger than 40 ns, the signal region is also clearly separated from the cross-talk signals whose ToT values are distributed around 25 ns.

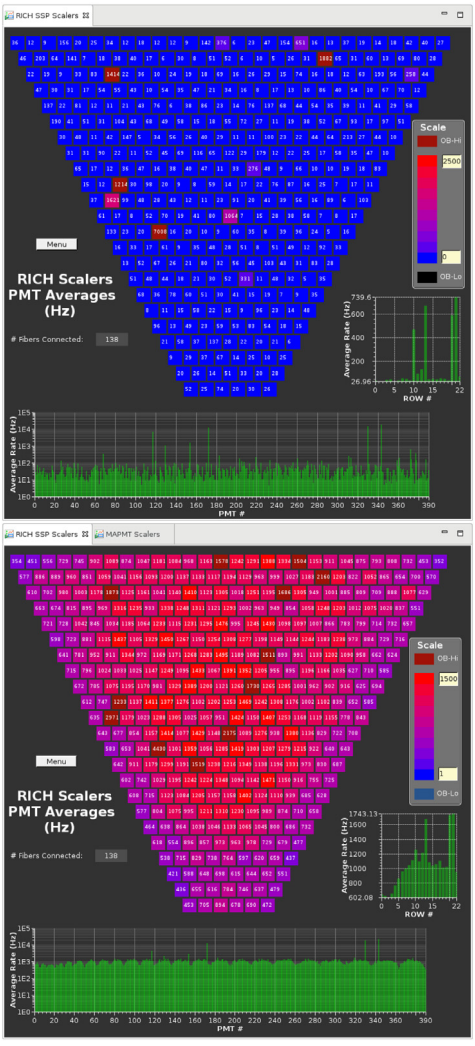

Fig. 29. The average count rates (in Hz) over 64 pixels for each MaPMT during data taking. Top: without beam on target, Bottom: with beam.i High counts rates in absence of beam are typically due to a single hot channel in the MaPMT.

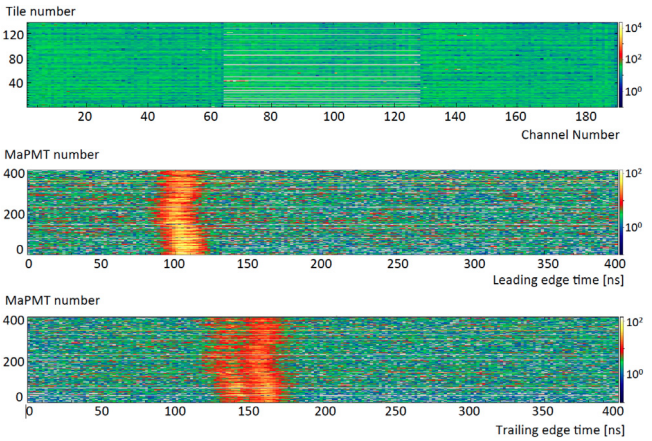

Fig. 30. Online monitor plots of the TDC occupancy with beam on. From top to bottom: channel occupancy in terms of the tile vs. channel number; leading edge time distributions per MaPMT; trailing edge time distribution per MaPMT.

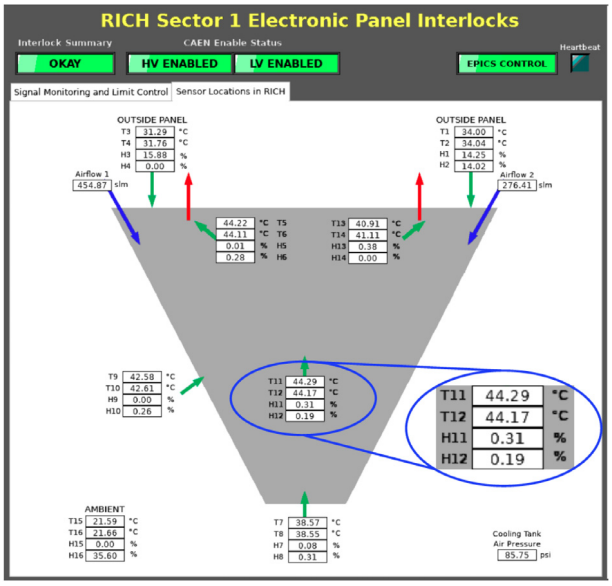

Fig. 31. Location and measured values of the temperature and humidity sensors inside the electronics panel, and the cooling air input flow as measured by the flow meters of the gas line.

After these tests, the common discriminator thresholds were set to +25 DAC units above the average MaPMT pedestal position, a level that corresponds to a small fraction of the average SPE amplitude.

4.3. RICH slow controls and interlocks

The RICH slow controls are based on Experimental Physics Industrial Control System (EPICS) [23]. It includes EPICS input–output controllers (IOCs) interfacing with different types of hardware via communication protocols and over 25k RICH process variables (PVs). The controls system monitors many aspects of the RICH detector, such as the scaler rates of all 25k Hamamatsu MaPMT pixels, the FPGA temperatures of each readout board, the HV and LV power supplies, the LV and current consumption of each readout unit, the gas system, and the temperature and humidity of the electronics panel volume and detector volume. For the Graphical User Interface (GUI), the Control Systems Studio (CS-Studio), an Eclipse-based suite of tools for developing and monitoring large-scale control systems, is used.

The quality of the data is monitored by scaler and TDC plots. Fig. 29 shows the average MaPMT rate measured by the scaler readout system when the beam is off (top plot) and when the beam is on (bottom plot). In the top plot, the few MaPMTs where the dark rate is substantially higher than the average can easily be seen. This is typically due to a single hot pixel in the MaPMT. The bottom plot shows that when the beam is on the rate is always dominated by physics events. Fig. 30 shows the occupancy plots from the TDC readout. The top plot shows the occupancy per channel, and the center and bottom plots show the distributions of the leading and trailing edge times per MaPMT, respectively. All of these plots are used during the data taking to identify possible malfunctioning channels and, eventually, restore them through a recovery procedure.

The slow controls and monitoring of the RICH detector is enforced by the hardware interlock system based on the National Instruments CompactRIO (cRIO) [24]. The cRIO system monitors the following parameters:

- Temperature and humidity in 16 locations of the detector volume;
- Temperature and humidity in 16 locations of the electronics panel;
- Air tank pressure;
- Air and nitrogen flow.

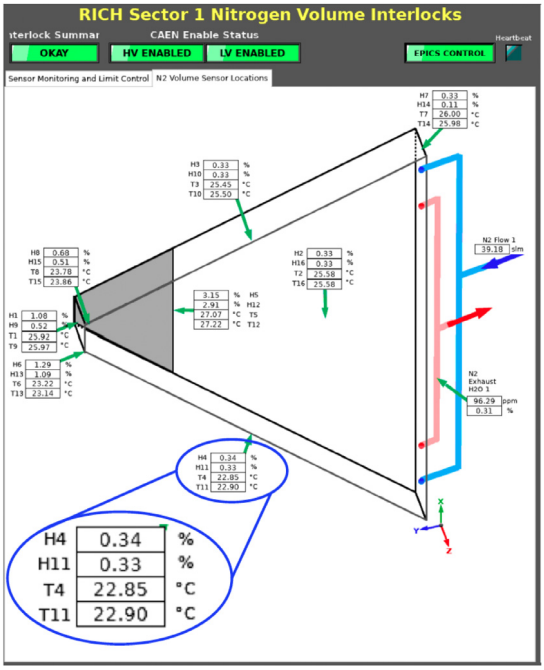

Fig. 32. Location and measured values of the temperature and humidity sensors inside the nitrogen volume, and the nitrogen input flow as measured by the flow meters of the gas line.

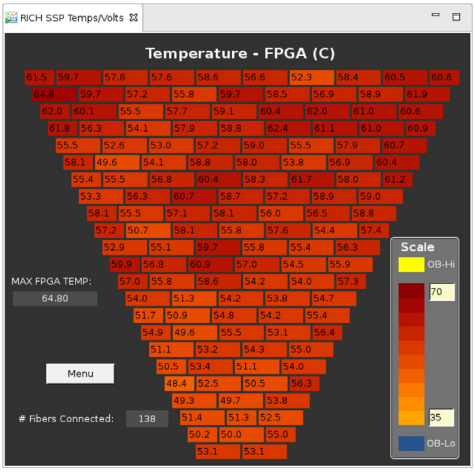

Fig. 33. Slow controls display: Map of the temperatures measured on the FPGA chips.

The locations of the temperature and humidity sensors, and the air and nitrogen flows fed into the electronics panel and nitrogen volume are shown in Figs. 31 and 32, respectively. The inner temperature of the electronics panel ranges between 38.5 °C and 44.5 °C moving from the bottom towards the top of the module, whereas the external temperature stays below 34.5 °C, in accordance with the requirement to not drive the FTOF system above 40 °C. The relative humidity is below 0.5%. In the nitrogen volume, the temperature ranges between 23 °C and 27 °C. The relative humidity is below 1.3% except in the central point close to the spherical mirror pivot, where it reaches a 3% value.

The signal levels are controlled by setting limits. If the temperatures, air flow, or air pressure go out of limits, the HV and LV are powered off, i.e. interlocked. In case the humidity or the nitrogen flow are out of limits, an alarm signal is generated.

Important safety parameters of the RICH detector are: the temperature of the front-end electronics, the gas flow, and the RICH internal relative humidity. Fig. 33 presents the map of the temperatures of the front-end electronics. Typical temperature values are around 65 °C on the FPGA chips and 40 °C inside the electronics panel volume. The safety temperature limits are 85 °C for the FPGAs, 80 °C for the optical fiber cables, and 40 °C for the temperature on the FTOF detector, which is about 10 cm away from the RICH. Therefore, the maximum allowed temperature was set to 75 °C on the FPGA and to 45 °C inside the electronics panel volume.

The nitrogen flow and the RICH internal relative humidity are measured by several probes installed inside the detector. An alarm is sent out in case the humidity exceeds 5% or in case the nitrogen flow drops below the normal value. In the latter case, the backup system starts working to restore the normal flow level and to ensure safe humidity conditions. During RICH operation, the humidity level has proven to be very stable with time.

5. The initial performance of the RICH detector

5.1. RICH event reconstruction

The RICH reconstruction is organized in four steps. In the first step, the spatial and time information of each hit in the MaPMTs is corrected by the spatial misalignment and time calibration parameters. The hits are ordered as a function of their ToT value, as this reflects the corresponding amplitude (released charge). A 3 × 3 MaPMT pixel matrix centered around a local maximum, i.e. the hit with the highest local ToT, is called a nonet. If more than 3 hits are found in the same nonet they are grouped into a RICH cluster. A cluster is typically generated by a charged particle producing Cherenkov light in the MaPMT window or ionization in the sensor dynode structure. If a sole hit is found close to a local maximum with a ToT lower than 80% of that maximum, the hit is flagged as possible cross-talk. Hits belonging to the same nonet of the local maximum are flagged as optical cross-talk, while hits readout by an electronics channel adjacent to the maximum hit in the MAROC chip are flagged as electrical cross-talk. Note that the readout circuit routing has been designed to connect anodes close in space to non-adjacent MAROC3 inputs. The above selection rejects about 87% of the cross-talk hits, as can be seen in Fig. 34. In the figure, the ToT distribution of the recorded RICH hits (black solid line) is shown together with the distributions of the hits identified as optical (magenta dash-dotted line) or electrical (green dashed line) cross-talk. The shoulders on the right of the cross-talk peaks are likely due to signal discharges wrongly identified as cross-talk. The hits selected for further analysis are highlighted by the dotted (blue) histogram. The excess at low ToT values indicates a residual contamination of unidentified cross-talk. The leftover cross-talk contamination, at the level of 2.7% of the signal, can be further reduced only with a time versus amplitude analysis, see Section 5.2. The cross-talk selection also removes a small (0.8% fraction) of true Cherenkov signals. Those correspond to MaPMT discharges that undergo incomplete dynode multiplication, while being by chance close in space to another Cherenkov signal. Hits flagged as cross-talk are not considered further in the RICH reconstruction.

The second step consists in finding the spatial match between the RICH clusters and the CLAS12 charged particle tracks. This requires that the extrapolated impact point of the track on the MaPMT plane is within 10 cm of the cluster center. The latter is calculated as a weighted average – with the ToT value as the weight – of the spatial coordinates of all the hits in the cluster. Matched clusters allow a precise study of the MaPMT detector position and orientation relative to the CLAS12 tracking system. This is shown in Fig. 35, where the distance between the RICH clusters and the matched drift chamber tracks [25] divided by the pixel spatial RMS, a sort of χ^2 distribution, is reported. The black distribution is before and the red one is after the alignment procedure.

The third step is the core of the RICH reconstruction [26]. For each hit in the MaPMT plane, an estimate of the corresponding Cherenkov angle is derived by ray-tracing the photon path inside the RICH volume

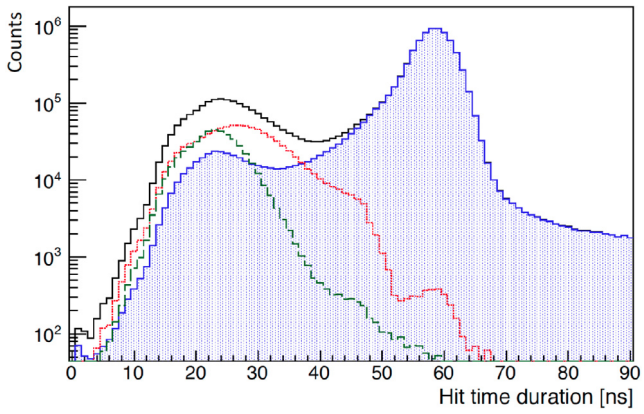

Fig. 34. ToT distribution of the recorded RICH hits (black solid line) together with the optical (magenta dash-dotted line) and electrical (green dashed line) cross-talk distributions. The hits selected for further analysis are highlighted by the blue dotted histogram.

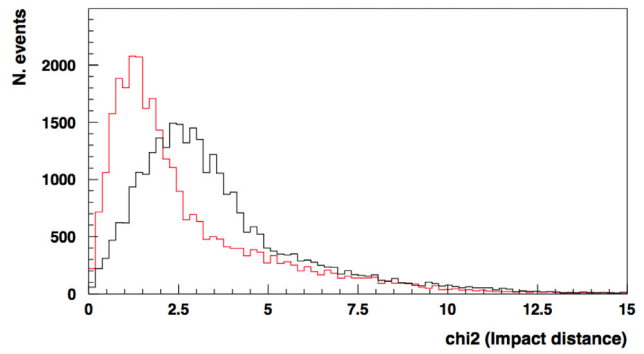

Fig. 35. RICH matching χ^2, defined as the distance between the RICH clusters and the matched drift chamber tracks divided by the pixel spatial RMS. The black distribution is before and the red one is after the alignment procedure. (For interpretation of the references to color in this figure legend, the reader is referred to the web version of this article.)

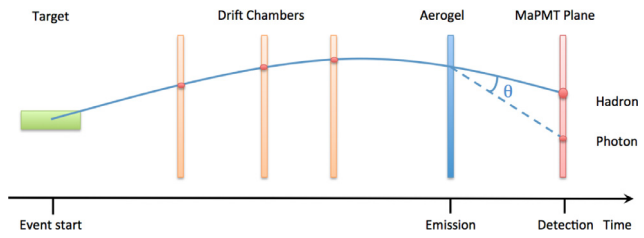

Fig. 36. The RICH photon detection time as measured by the CLAS12 spectrometer. It is defined as the event start time plus the flight-times of the hadron from the interaction point to the radiator center and of the ray-traced photon within the RICH volume.

taking into account possible reflections. This is done in turn for each charged particle traced through the RICH, with the photon emission point assumed to be the middle point of the particle path inside the aerogel radiator. In the fourth step, a particle identification algorithm is applied using an event-based likelihood of the reconstructed Cherenkov angles and times.

5.2. RICH time resolution

The time information of the RICH hits is provided by the leading edge time T_l measured by the TDC implemented into the FPGA board with a 1-ns precision. In-time photon hits are selected by comparing their T_l with the time T_{calc} computed using the CLAS12 information (see Fig. 36). T_{calc} comprises the event start time, the charged

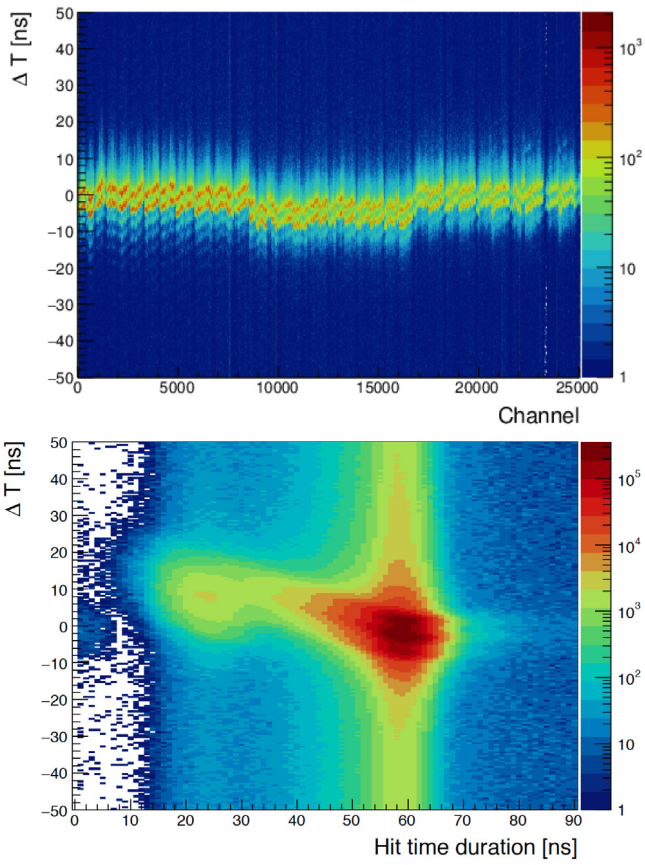

Fig. 37. Top plot: distribution of the time difference ΔT between the measured RICH and calculated CLAS12 times as a function of the RICH readout channel. Bottom plot: cumulative distribution of the time difference ΔT as a function of the hit duration time (ToT).

track path and flight time provided by the tracking system, and the Cherenkov photon path reconstructed inside the RICH as explained in Ref. [26]. Being based on the precise FTOF system [3] and the accelerator RF frequency, the CLAS12 computed time features a time resolution on the order of 100 ps, significantly better than RICH. The CLAS12 computed time can therefore be used as a reference for the RICH time calibration.

With respect to the expected time resolution, significant channel-by-channel variations are found in the difference between the measured and the calculated times as shown in the top plot of Fig. 37, where the distribution of $\Delta T = T_l - T_{calc}$ as a function of the channel number is shown. These variations are introduced by the readout chain, with the biggest contribution coming from the average length of the 3 optical DAQ fiber trunks and from the specific length of the various fibers in each trunk. Smaller variations among the individual channels of one board can also occur due to the different circuit routing and components. An additional overall time constant is expected from the relative calibration of the RICH with respect to the rest of the CLAS12 detectors.

A broadening of the ΔT distributions is due to the time walk, i.e. the dependence of the trailing edge time on the amplitude of the input signal. Since the MAROC3 readout mostly works in the saturated regime already at the SPE level, this effect is expected to be relevant for small amplitude signals, as can be seen from the bottom plot of Fig. 37. Saturated signals have typical ToT values on the order of 60 ns, while small amplitude signals are expected to be discriminated up to several ns later. The vertical band at ToT≈60 ns comprises a distribution of random-time MaPMT dark counts and off-time beam

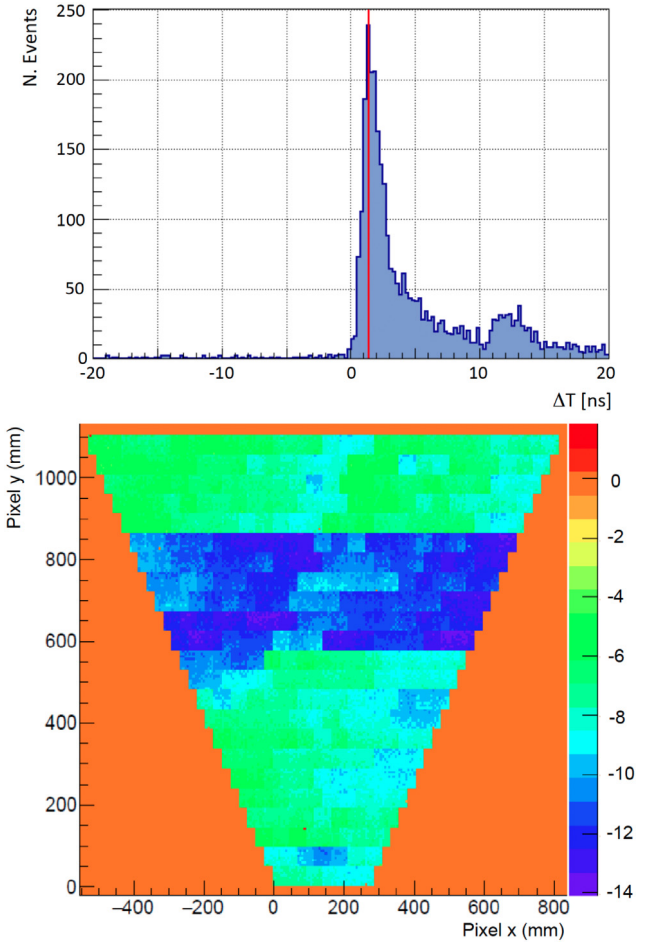

Fig. 38. Top plot: ΔT distribution for one readout channel; the red line indicates the time offset value. Bottom plot: typical map of the time offsets. (For interpretation of the references to color in this figure legend, the reader is referred to the web version of this article.)

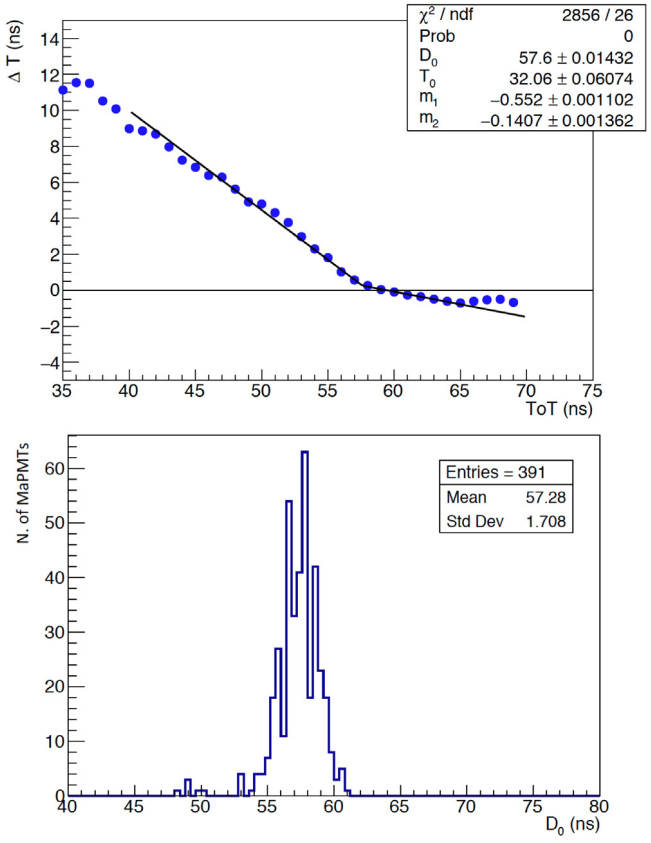

Fig. 39. Top plot: fit of the time-walk correction for one MaPMT. Bottom plot: distribution of the ToT saturation values extracted from the time-walk corrections.

bunches. The independent excess around ToT≈25 ns signals a residual contamination of cross-talk pulses as anticipated in Section 5.1.

A two-step calibration procedure was implemented in order to align the time measured from all RICH readout channels with the expected (calculated) one. The current version of the software uses electrons and charged pions identified in CLAS12 with momenta larger than 2.5 GeV/c and Cherenkov photons reconstructed in the RICH with no reflections on the mirrors.

The first step of the procedure consists in the evaluation of the 25024 time offset corrections. The values of ΔT are plotted for each channel and the position of the maximum is taken as the time offset for that channel. The top plot of Fig. 38 shows a typical ΔT distribution, with a pronounced peak, a broad tail due to the time walk, and a small enhancement above ≈10 ns most likely due to residual cross-talk hits. The vertical line indicates the adopted value for the time offset correction. The bottom plot of Fig. 38 shows a typical map of the time offsets. Three regions of comparable values are highlighted, corresponding to the tiles connected to the 3 optical fiber trunks, on top of smaller channel-by-channel variations.

Once the individual channels were corrected for the time offsets, the time-walk corrections were extracted from the ΔT distribution as a function of ToT. Since the threshold level is common to all channels of one MAROC3 chip, and the amplitude equalization has been performed, one expects that the same time-walk correction should work for all channels of one MaPMT. This was verified by comparing plots like the one shown in the bottom plot of Fig. 37 for all channels of the MaPMTs. A set of 391 time-walk correction functions, one per MaPMT, is therefore extracted by fitting the dependence of ΔT as a function of ToT, as shown in the top plot of Fig. 39. The dependence is fit with two lines, one for the saturated regime and one for the linear region:

$$\begin{aligned} &\mathrm{ToT} < \mathrm{ToT}_0 \ : \ m_1 \mathrm{ToT} + \Delta \mathrm{T}_0 \\ &\mathrm{ToT} > \mathrm{ToT}_0 \ : \ m_2 \mathrm{ToT} + (m_1 - m_2)\mathrm{ToT}_0 + \Delta \mathrm{T}_0 \end{aligned} \tag{2}$$

The free parameters of the fit are the two slopes m_1 and m_2, the value ToT_0 where the two lines cross, i.e. the ToT saturation value, and the value $\Delta \mathrm{T}_0$ at zero ToT. The data show small deviations from the linear behavior. However, such a simple functional form was adopted to minimize the probability of fit failure (having to deal with several hundreds of fits) and because it was proven to be enough to achieve time resolutions that meet the specifications. In the bottom plot of Fig. 39, a typical distribution of the saturation ToT values obtained from the fit is shown. The average value is around 57 ns with small variation from MaPMT to MaPMT.

After calibration, the corrected ΔT distribution is centered at zero for all channels, see Fig. 40. As a consequence, a few ns time coincidence can be applied to remove the spurious hits. As shown in the bottom panel of Fig. 40, the cross-talk hits at ToT ≈25 ns and the 4.008 ns sub-structure of the off-time beam bunches at ToT≈60 ns become clearly visible. A typical ΔT distribution is shown in Fig. 41, where the red and black histograms show the ΔT values before and after the correction, respectively. The red curve is a Gaussian fit of the corrected distribution. On average, we obtained a time resolution $\langle\sigma\rangle$ ≈0.7 ns, well below the requirement of 1 ns.

5.3. RICH Hadron separation

The RICH has been designed to provide hadron identification in the 3 GeV/c to 8 GeV/c momentum range. The most challenging separation

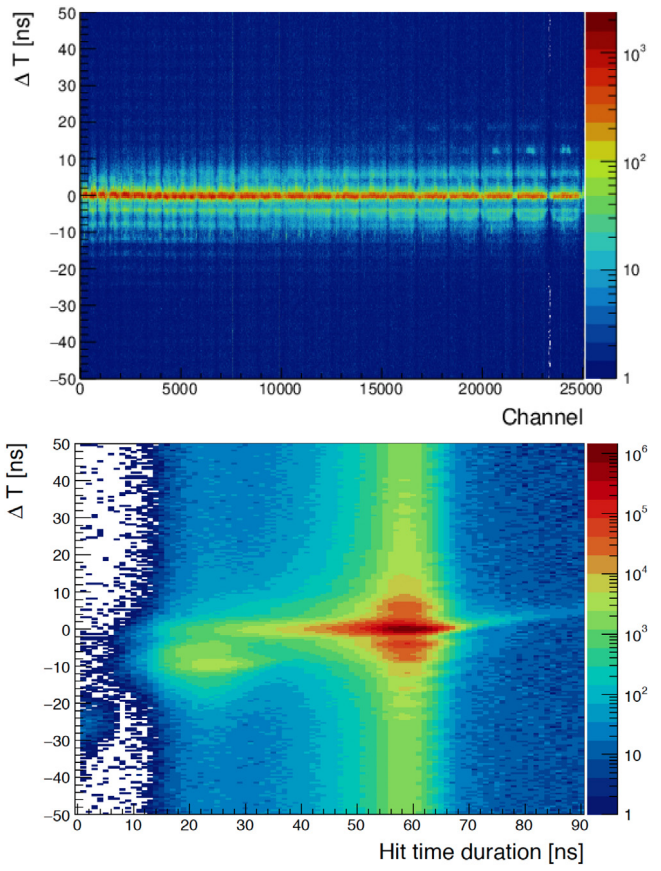

Fig. 40. Distribution of the time difference ΔT between the measured RICH and extrapolated CLAS12 times after the time calibration. On the top as a function of the readout channel; on the bottom as a function of the signal amplitude ToT.

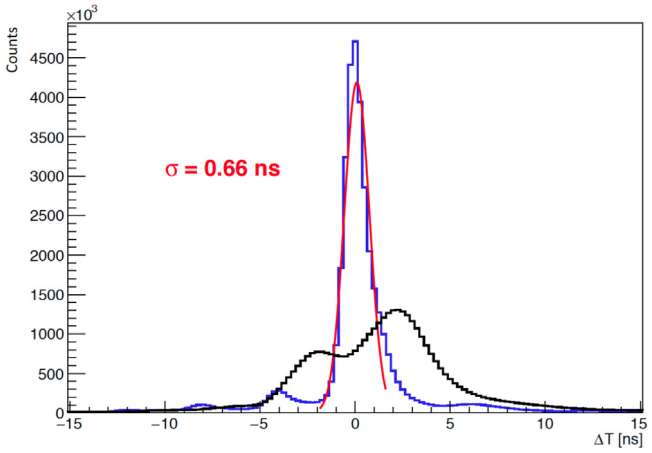

Fig. 41. Typical ΔT distribution before (black) and after (blue) the time-walk correction for all RICH pixels. The red line is a Gaussian fit of the corrected distribution, with a global width $\sigma = 0.66$ ns. (For interpretation of the references to color in this figure legend, the reader is referred to the web version of this article.)

is between kaons and pions, as their Cherenkov angles become closer and closer with the increase of momentum until a minimum difference of 6 mrad at 8 GeV/c. In addition, in this momentum range the pion yield is more than an order of magnitude larger than for the other hadron species. The RICH Cherenkov angle reconstruction relies on the performance of the CLAS12 tracking system, able to provide tracks with momentum resolution better than 1% and polar angle resolution better than 1 mrad [4].

Various ring imaging topologies are possible due to the unconventional RICH geometry. These topologies are generated by direct photons in proximity focusing and by reflected photons in mirror focusing geometries. In the momentum range of interest (between 3 GeV/c and 8 GeV/c), electrons can be used for a detailed optimization of the RICH performance since, being in a saturated regime, their Cherenkov angles are indistinguishable from those of pions. The work is still ongoing to make use of the large recorded electron statistics.

Examples of reconstructed RICH events are shown in Figs. 42–45 for particles identified as electrons by CLAS12. In each figure, the reconstructed RICH event is displayed on the left. The ray-tracing approach allows, for each particle hypothesis, to anticipate the expected photon pattern and the associated hits on the photodetectors, indicated by the small dots in the figures. The measured RICH hits are shown as open circles, whereas the reconstructed photon hits are shown as the full symbols. Direct and reflected photons are indicated in magenta circles and blue squares, respectively. A remarkable feature of the RICH detector is the low level of spurious hits from accidentals, in-time background (i.e. Rayleigh scattering), and dark counts. This feature is crucial for the most challenging cases: particles with high momenta close to the 8 GeV/c limit that require the best resolution in Cherenkov angle, and particles pointing towards the spherical mirror whose number of detected photons is limited by the double reflection and a second passage through the radiator.

For each event, the details of the time and Cherenkov angle reconstruction are shown on the right. On the top panel, the time coincidence ΔT between the RICH measured hit and the CLAS12 calculated time is displayed as a function of the photon flight time within the RICH (photon transit time). The time coincidence ΔT should be close to zero for any true photon path. As a consequence, a valid photon reconstruction is initially selected by requiring $\Delta T < 3$ ns, indicated by the horizontal dashed lines. The photon path length is represented by the transit time inside the RICH, from the emission point within the aerogel to the detection point in the MaPMT plane after all possible reflections. Photons reflected by the spherical mirror and directed back to the aerogel travel twice the gap, with an expected significant increase of path length and a corresponding distinctive ≈6 ns longer transit time.

In the bottom panel, the measured angles are compared to the expected distributions for different particle hypotheses. The width of each distribution corresponds to the expected SPE angular resolution, while the average value depends on the particle type and momentum. An acceptance range is defined from the smallest angle expected for a proton to the largest angle expected for an electron, enlarged by three times the expected angular resolution. For the latter, a conservative value of 6 mrad is taken for the single photon case. These limits are indicated by the vertical dashed lines.

For each reconstructed photon path an estimate of the corresponding Cherenkov angle is obtained and histogrammed on the plot. In all cases studied, both reflected and direct photon information is consistent with the electron hypothesis. In particular, the reconstructed reflected and direct photon paths with ΔT close to zero provide Cherenkov angle values consistent with an electron, as expected. The narrow distribution of the measured angle values indicate that kaons can clearly be separated up to momenta greater than 6 GeV/c. Electrons can be distinguished from pions only at low momenta, below 2 GeV/c.

Each aerogel tile presents specific features because the challenging production process, tuned to achieve the highest transparency over a large volume, is not fully industrialized. The most important quality parameters are the density, related to the average refractive index, homogeneity, related to the refractive index variations within the volume, and tile bending, originated by the inner material tension and related to the surface planarity. The effect of these features on the RICH photon reconstruction can be studied in detail using the control sample of electrons identified by CLAS12. Given the large number of tiles and the broad range of particle directions after the CLAS12 bending magnets, such a study requires large statistics and is still

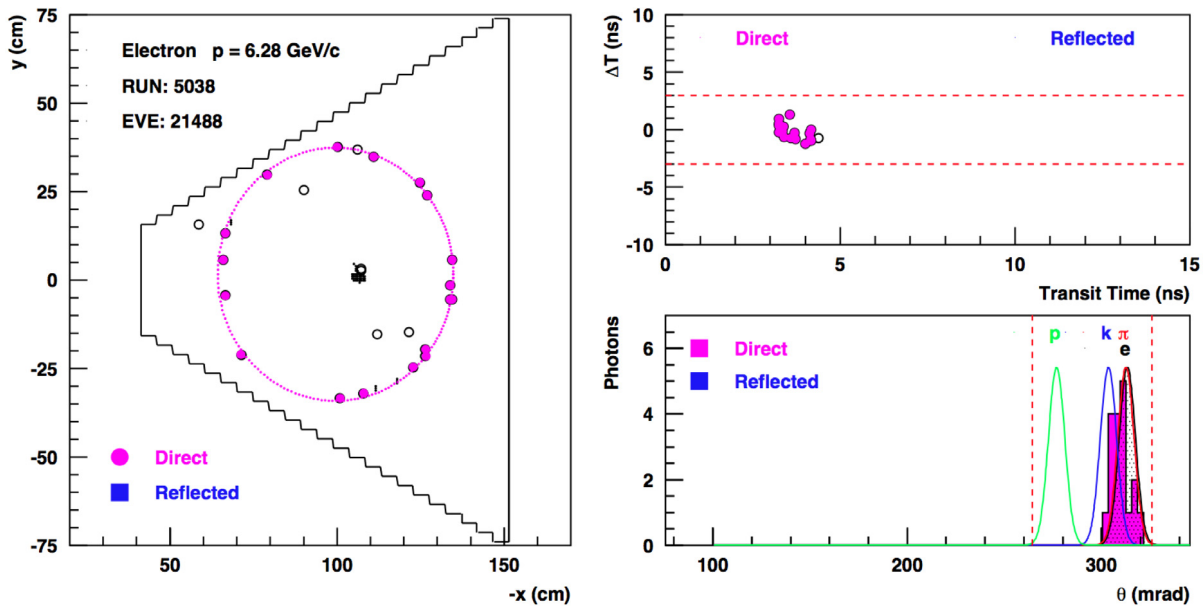

Fig. 42. Example of a reconstructed RICH event with only direct photons. On the left the event display, on the right the time (top) and angle (bottom) analysis. Refer to the text for details.

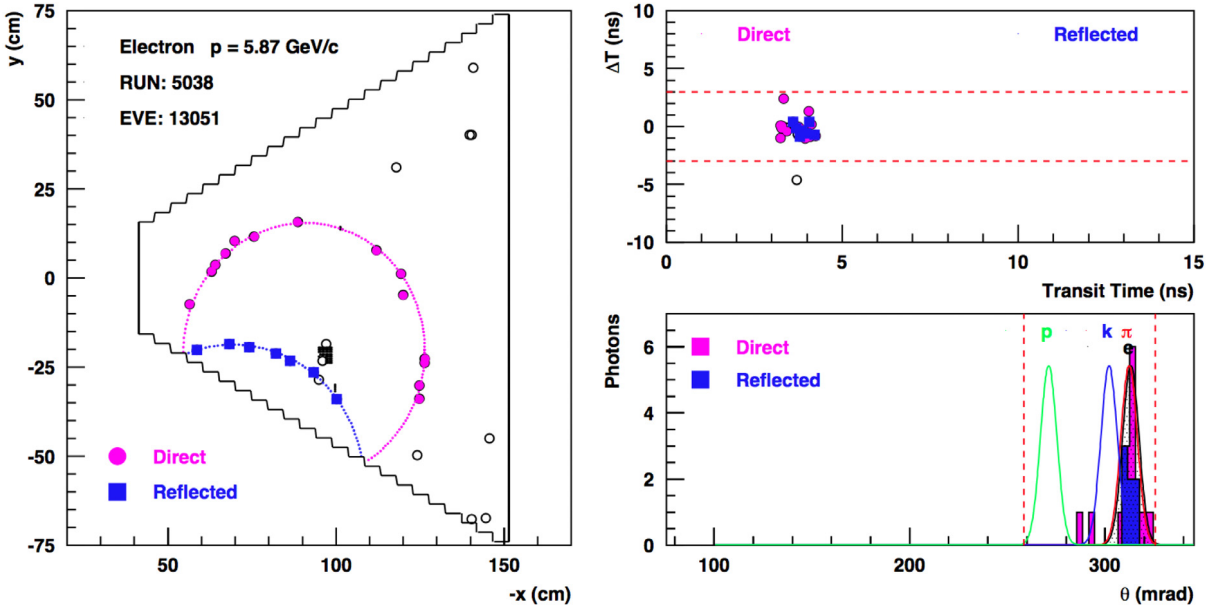

Fig. 43. Example of a reconstructed RICH event with a partial ring reflected by the lateral flat mirror. On the left the event display, on the right the time (top) and angle (bottom) analysis. Refer to the text for details.

ongoing. A similar approach is used for the alignment study. Also in this case, large statistics are needed due to the numerous involved components (aerogel layers, mirrors, and MaPMT plane) and photon path configurations.

As a general approach, the RICH performance is studied separately for each aerogel tile. The RICH global performance estimators are then defined by averaging the results over all the radiator tiles. Despite the fact that the above studies have not yet been finalized, and only partial corrections have been implemented so far, the preliminary SPE Cherenkov angle resolution yields typical values around 6 mrad. It is expected to improve towards the goal value of 4.5 mrad once the corrections for the detector misalignment are implemented and the realistic optical parameters of each aerogel tile are taken into account.

As an example, the effect of a preliminary alignment of the RICH as a whole is shown for one aerogel tile in Fig. 46. The resolution is calculated as the RMS of the distribution of the average Cherenkov angles extracted for each single track of the electron control sample. Such averages are calculated over the detected photons, whose reconstructed path satisfies the time coincidence and provides an angle within the kinematic limits described above, associated with the track. The fit shown uses the function

$$\sigma = \sqrt{\frac{\sigma_1^2}{N} + \sigma_0^2}$$

to extract the single photon resolution σ_1 in addition to a constant term σ_0 measuring the residual systematics due, e.g. to misalignment. After (a preliminary) alignment, the resolution improves toward the design values, which are 4.5 mrad for single photon detection and 1.5 mrad for the average over all the photons that are associated with the control electron track. As it is shown in Figs. 47–49, the preliminary

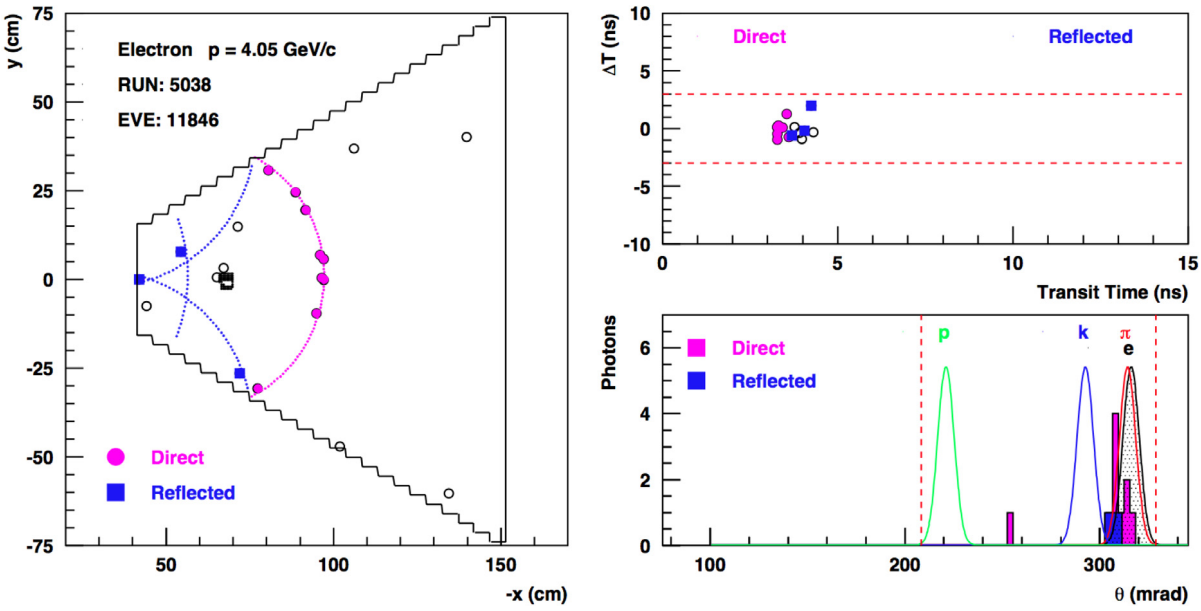

Fig. 44. Example of a reconstructed RICH event with photons reflected by all the lateral mirrors. On the left the event display, on the right the time (top) and angle (bottom) analysis. Refer to the text for details.

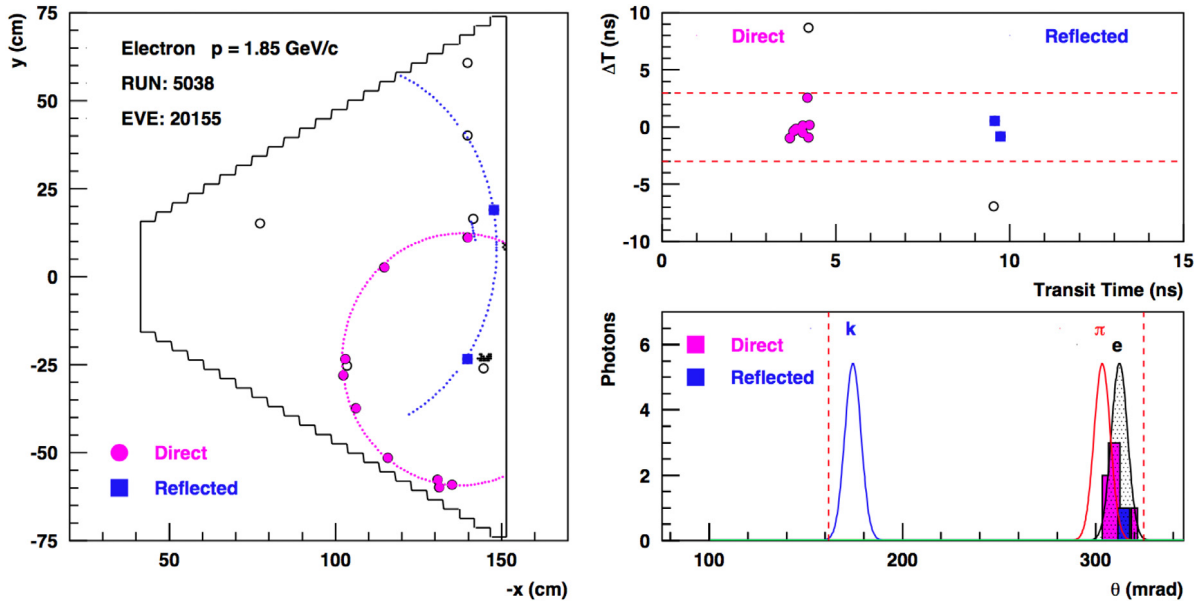

Fig. 45. Example of a reconstructed RICH event with a partial ring reflected back by the spherical mirror and passing twice the aerogel layer. On the left the event display, on the right the time (top) and angle (bottom) analysis. Refer to the text for details.

Cherenkov angle resolution is sufficient for hadron separation in the required momentum range from 3 GeV/c to 8 GeV/c. As expected for electron particles identified in CLAS12 by the gas Cherenkov counter HTCC and the calorimeter, the RICH reconstructed Cherenkov angle is saturated to the maximum value in the whole momentum range, see Fig. 47. For positive particles not identified as positrons by other detectors, the RICH measured Cherenkov angles concentrate around the expected values for pion, kaon, and proton particles depending on their momentum, see Fig. 48. The three hadron populations are separated over the whole momentum range, see Fig. 49.

6. Conclusions

A RICH detector has been designed to enhance the hadron identification capability at CLAS12 in the 3 GeV/c to 8 GeV/c momentum range. It substitutes the baseline LTCC gas threshold Cherenkov detector in two of the CLAS12 sectors, to create a symmetric left–right setup optimized for running with polarized targets. The first module was installed at the beginning of 2018, in time for the start of the experiment data taking. The second module is under construction and expected to be ready in the summer 2021, in time for the first run with polarized targets.

To efficiently cover the desired momentum range, the RICH employs innovative technological solutions. Among these are composite aeronautic light-materials to ensure the needed mechanical structure rigidity, aerogel radiators of unprecedented large volume (up to 200 × 200 × 30 mm^3) and high transparency (≈50 mm scattering length), light mirrors (of the order of 1% radiation length) made of carbon fiber or, for the first time in a nuclear experiment, glass-skin technology, and highly segmented and highly packed Hamamatsu

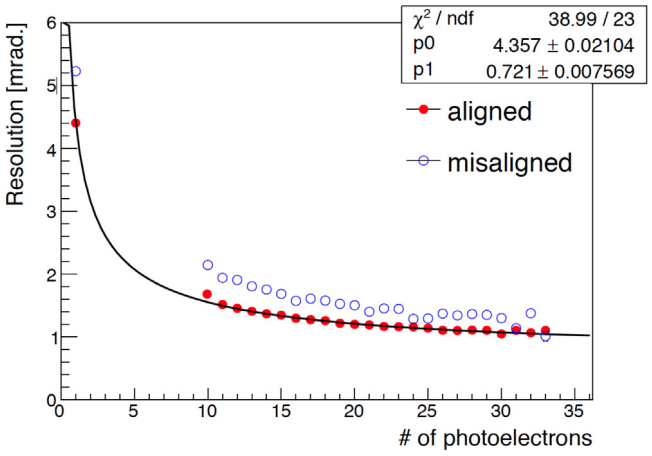

Fig. 46. RICH Cherenkov resolution before (open points) and after (solid points) a preliminary RICH alignment. The whole RICH detector is aligned minimizing the matching distance between the RICH clusters and the extrapolated drift chamber tracks. No possible misalignment of a single RICH component is accounted for. The distribution is for particles passing through one aerogel tile of 2-cm thickness (tile 12 in layer 1) and for direct photons.

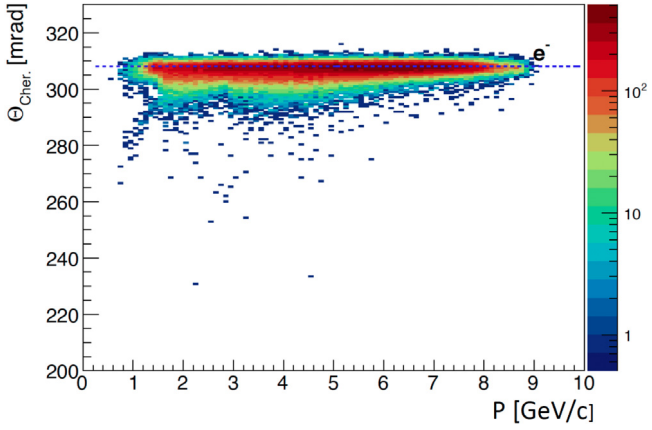

Fig. 47. RICH response for electrons as identified by CLAS12. As expected, the measured Cherenkov angle is saturated over the whole momentum range, from 3 GeV/c up to 8 GeV/c. The distribution is for particles passing through one aerogel tile of 2-cm thickness (tile 12 in layer 1) and direct photons.

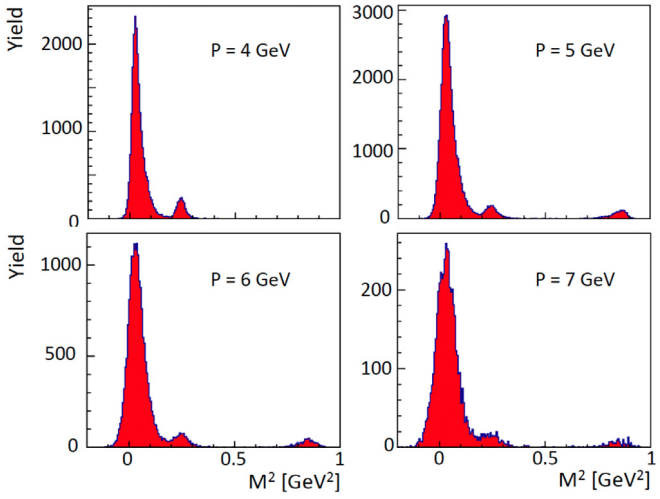

Fig. 49. RICH response for non-electron particles in slices of momentum, from 4 GeV/c up to 7 GeV/c.

H8500 and H12700 multi-anode photomultipliers. A compact and scalable readout electronics system has been realized for the detector, able to discriminate Cherenkov signals down to as small as a 1/32 fraction of the single photon amplitude, with excellent efficiency and stability, and a time resolution better than 1 ns.

The peculiar geometry of the CLAS12 sector suggested an innovative hybrid-optics solution to limit the active area to ≈1 m^2 per sector, with part of the light directly imaged and part of the light detected after reflection from mirrors. This and the bending into the torus field of the CLAS12 Forward Detector create a variety of possible topologies for the particle and photons paths. The RICH reconstruction exploits a ray-tracing algorithm to provide a Cherenkov angle estimation for each photon hit and hadron track in the event. This basic experimental information allows an independent development of higher-level PID algorithms with increasing sophistication.

Preliminary data analysis shows that the CLAS12 RICH is able to match the required time and Cherenkov angle resolutions. After calibration, each of the 25k channels features a time resolution of the order of 0.6 ns, better than the 1 ns specification. High-momentum particles define the most stringent requirements for the RICH performance. As the pion yield is larger than the other particles species by an order of magnitude, a 4σ angle separation is required to contain the contamination at the percent level. At 8 GeV/c, this implies an angle resolution

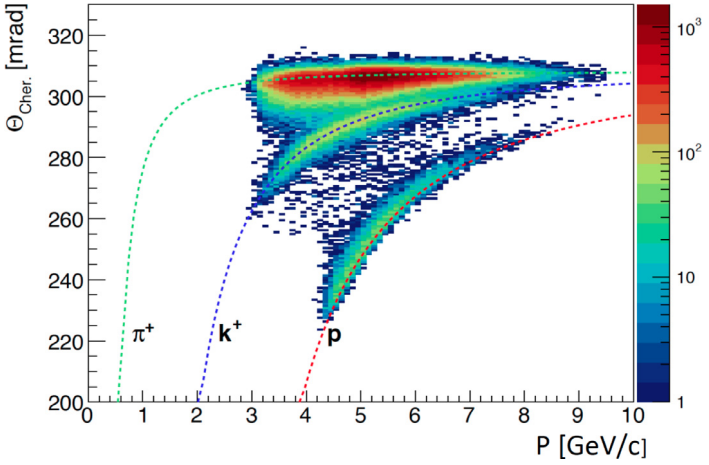

Fig. 48. RICH response for non-electron particles as defined by CLAS12. The measured Cherenkov angles distribute around the expected values for pion, kaon, and proton hypotheses as a function of their momentum. The three hadron populations are separated over the whole momentum range, from 3 GeV/c up to 8 GeV/c. The distribution is for particles passing through one aerogel tile of 2-cm thickness (tile 12 in layer 1) and spanning the entire momentum range of interest for RICH.

of 1.5 mrad. Despite the fact that the detailed study of the alignment and optical performance of the various components is still ongoing, the detector has already demonstrated a single-photon angle resolution better than 5 mrad and an average number of 19 photons per charged particle in the forward high-momentum direction, in line with the detector design specifications. This reflects in an angle resolution per charged particle close to the design value of 1.5 mrad and an effective hadron identification capability over the entire required momentum range.

Declaration of competing interest

The authors declare that they have no known competing financial interests or personal relationships that could have appeared to influence the work reported in this paper.

Acknowledgments

This material is based upon work supported by INFN under the MIUR priority project CLASMED, Italy and by the U.S. Department of Energy, Office of Science, Office of Nuclear Physics under contract DE-AC05-06OR23177 and the National Science Foundation, Award #1615067. We thank the JLab Detector Support Group and Fast Electronics Group, the Hall B technical and management staff, and the INFN technical and administrative service.

References

[1] Y. Sharabian, et al., The CLAS12 high threshold Cherenkov counter, Nucl. Instrum. Methods A (2020) in this issue.
[2] M. Ungaro, et al., The CLAS12 low threshold Cherenkov counter, Nucl. Instrum. Methods A (2020) in this issue.
[3] D.S. Carman, et al., The CLAS12 forward time-of-flight system, Nucl. Instrum. Methods A (2020) in this issue.
[4] V.D. Burkert, et al., The CLAS12 spectrometer at Jefferson laboratory, Nucl. Instrum. Methods A (2020) in this issue.
[5] G. Asryan, et al., The CLAS12 forward electromagnetic calorimter, Nucl. Instrum. Methods A (2020) in this issue.
[6] M. Contalbrigo, et al., The large-area hybrid-optics CLAS12 RICH detector: Tests of innovative components, Nucl. Instrum. Methods A 766 (2014) 22.
[7] M. Contalbrigo, et al., Aerogel mass production for the CLAS12 RICH: Novel characterization methods and optical performance, Nucl. Instrum. Methods A 876 (2017) 168.
[8] E. Aschenauer, et al., Optical characterization of n = 1.03 silica aerogel used as radiator in the RICH of HERMES, Nucl. Instrum. Methods A 440 (2000) 338.
[9] http://www.compositemirrors.com/.
[10] G.J. Barber, et al., Development of lightweight carbon-fiber mirrors for the RICH 1 detector of LHCb, Nucl. Instrum. Methods A 593 (2008) 624.
[11] C. D'Ambrosio, et al., Precision optical systems for the new generation of ring imaging Cherenkov detectors in high energy physics experiments, Nucl. Instrum. Methods A 478 (2002) 344.
[12] https://www.evaporatedcoatings.com/.
[13] http://www.media-lario.com/.
[14] https://www.hamamatsu.com/resources/pdf/etd/H8500_H10966_TPMH1327E.pdf.
[15] R.A. Montgomery, et al., Multianode photomultiplier tube studies for imaging applications, Nucl. Instrum. Methods A 695 (2012) 326.
[16] S. Anefalos Pereira, et al., Test of the CLAS12 RICH large scale prototype in the direct proximity focusing configuration, Eur. Phys. J. A 52 (2016) 23.
[17] https://www.hamamatsu.com/resources/pdf/etd/H12700_TPMH1348E.pdf.
[18] M. Contalbrigo, et al., Single photon detection with the multi-anode CLAS12 RICH detector, Nucl. Instrum. Methods A 952 (2020) 16123.
[19] S. Blin, et al., MAROC, a Generic Photomultiplier Readout Chip, in: IEEE Nucl. Sci. Symp. Conf. Rec. Vol. 2010, 2010, p. 1690.
[20] S. Boyarinov, et al., The CLAS12 data acquisition system, Nucl. Instrum. Methods A (2020) in this issue.
[21] Pavel Degtiarenko, Precision analysis of the photomultiplier response to ultra low signals, Nucl. Instrum. Methods A 872 (2017) 1.
[22] P. Degtiarenko, V. Kubarovsky, A. Kim, A. Smith, to be published.
[23] Experimental Industrial Physics Control System, https://epics-controls.org.
[24] https://www.jlab.org/div_dept/physics_division/dsg/notes/2016-012%20National%20Instruments%20compactRIO-based%20control,%20monitoring,%20and%20interlock%20system.pdf.
[25] M.D. Mestayer, et al., The CLAS12 drift chamber system, Nucl. Instrum. Methods A (2020) in this issue.
[26] V. Ziegler, et al., The CLAS12 software framework and event reconstruction, Nucl. Instrum. Methods A (2020) in this issue.